Marine and Petroleum Geology 167 (2024) 106941

Contents lists available at ScienceDirect

Marine and Petroleum Geology

journal homepage: www.elsevier.com/locate/marpetgeo

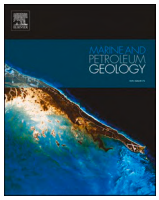

Unraveling marine phosphogenesis along the Miocene coast of Peru: Origin and sedimentological significance of the Pisco Formation phosphorites

Giulia Bosio [a,b,*,1], Anna Gioncada [b,1], Elisa Malinverno [a], Giovanni Coletti [a], Alberto Collareta [b], Luca Mariani [a], Alessandro Cavallo [a], Giovanni Bianucci [b], Mario Urbina [c], Claudio Di Celma [d]

[a] Dipartimento di Scienze dell'Ambiente e della Terra, Università degli Studi di Milano-Bicocca, 20126 Milano, Italy
[b] Dipartimento di Scienze della Terra, Università di Pisa, 56126 Pisa, Italy
[c] Departamento de Paleontología de Vertebrados, Museo de Historia Natural, Universidad Nacional Mayor de San Marcos, Lima 1, Peru
[d] Scuola di Scienze e Tecnologie, Università di Camerino, 62032 Camerino, Italy

ARTICLE INFO

Keywords:
Phosphorite
Unconformity
Sedimentary condensation
Apatite
REE
East pisco basin
Marine geochemistry
Upwelling

ABSTRACT

Phosphorite deposits form through phosphogenesis, a mechanism of diffusion and concentration of interstitial phosphate in sediments leading to Ca-phosphate mineral precipitation in a favorable sedimentary regime at the seafloor. Stretching along the Peruvian coast, the East Pisco Basin is known to host phosphorite beds of Miocene age. In this study, we investigate the petrographic, mineralogical and chemical composition of the Miocene phosphorite layers of the East Pisco Basin, and discuss the phosphogenetic mechanism(s) and sedimentary dynamics that led to the genesis and accumulation of P-rich deposits. Phosphorite samples were collected from layers overlaying stratigraphic unconformities within the Pisco Formation and subsequently analyzed through multiple methods: optical microscopy, XRD, XRF, SEM-EDS, EPMA, ICP-MS and LA-ICP-MS. Our results indicate that these layers consist of phosphatic clasts and nodules along with dolomite clasts, basement boulders, shark teeth, mollusk molds and vertebrate bone fragments. The P-rich clasts are mainly composed of phosphatic intraclasts and small phosphatic nodules. They occur associated with minor amounts of dolomite clasts coated by Fe-oxyhydroxides and laminites. Clasts and nodules are cemented by both early and late diagenetic cements, such as dolomite, calcite, silica, gypsum/anhydrite and baryte. Our observations suggest that the Pisco phosphorite deposits are transgressive lags laying on ravinement surfaces. They formed just below the sediment-water boundary during the early transgression phases, when the porewaters were enriched in phosphorus due to the abundance of organic-rich sediments and the microbial activity, as typical of upwelling settings. These deposits formed in shallow marine conditions, characterized by high biological productivity and low net sedimentation rates, with suboxic conditions at and beneath the sediment-water interface. The concentration of phosphate-coated clasts was then favored by a sedimentary condensation mechanism of dynamic bypassing. Overall, this study provides new insights into the genesis of phosphorite layers in the East Pisco Basin and highlights the importance of understanding the complex interplay between authigenic and sedimentological processes in the formation of these economically and geologically relevant sedimentary rocks.

1. Introduction

Phosphorites, or phosphate rocks, are sedimentary deposits with high phosphorus (P, in the form of phosphate) concentrations (Filippelli, 2011). These deposits form via phosphogenesis, i.e., a mechanism of diffusion and concentration of interstitial phosphate in sediments, which in appropriate redox and pH conditions leads to the precipitation of authigenic Ca-phosphate minerals (Föllmi, 1996).

Interest in the study of phosphorites and the genesis of phosphatic deposits rose during the 1930s due to a rapid rise of the importance of phosphate rocks as industrial raw materials. In fact, from the late 19th century onward, the use of processed phosphatic mineral as fertilizers has grown continuously to become a worldwide agricultural practice during the Green Revolution, such that agriculture is now dependent on artificial fertilizers (Cordell et al., 2009). Nowadays, phosphate rocks are included in the 2023 EU list of Critical Raw Materials, based on their

* Corresponding author. Dipartimento di Scienze dell'Ambiente e della Terra, Università degli Studi di Milano-Bicocca, 20126 Milano, Italy.
E-mail address: giulia.bosio.giulia@gmail.com (G. Bosio).
[1] These authors contributed equally to this work.

https://doi.org/10.1016/j.marpetgeo.2024.106941
Received 1 March 2024; Received in revised form 2 June 2024; Accepted 5 June 2024
Available online 8 June 2024

economic importance and supply risk (Grohol and Veeh, 2023).

Today, with the increasing demand of Rare Earth Elements (REEs) for modern technologies, phosphorite deposits are gaining further economic significance due also to their ability of concentrating considerable amounts of these elements. According to Emsbo et al. (2015), phosphorites might be considered as a primary source of REEs, one that has the potential to account for the global REE supply shortage.

Past and present phosphogenesis has been reported from all over the world (Cook and Shergold, 1986; Notholt et al., 1989; Burnett and Riggs, 1990; Glenn et al., 1994; Baturin and Bezrukov, 1979; Baturin, 1982; Cook and Shergold (1986); Notholt et al. (1989); Burnett and Riggs (1990); Glenn et al. (1994); Föllmi, 1996, 2016; Pufahl and Groat, 2016). Zones of present-day formation of phosphate-rich sediments and phosphorites are mostly located in coastal upwelling areas, but some occur in nearshore and deltaic environments (Föllmi, 1996). Today, phosphogenesis is reported from along the Pacific American coasts (in Baja California and from Chile to Peru in the southern hemisphere), along the Atlantic African coasts (in Namibia and South Africa), in the Arabic Sea (western coasts of India) and along the eastern Australian coast. Several other Quaternary deposits are also known (e.g., from California, Florida, the northwestern coasts of the Iberian Peninsula and Africa, and New Zealand), however with no indications of ongoing phosphogenesis (Baturin, 1982; Cullen and Burnett, 1986; Föllmi, 1996, 2016). Ancient phosphorites are widely distributed worldwide and known to span chronostratigraphically from the Precambrian to the Quaternary (Baturin and Bezrukov, 1979; Sheldon, 1981; Papineau, 2010).

Along the Peru-Chile margin, the economic and scientific interest in phosphate deposits has sparked investigations especially from the 1970s onwards (Zen, 1959; Veeh et al., 1973; Manheim et al., 1975; Burnett, 1977, 1980; Burnett and Veeh, 1977; Suess, 1981; Burnett et al., 1982, 1983; McArthur, 1983; Frohlich et al., 1983, 1988; Baker and Burnett, 1988; Glenn and Arthur, 1988; Piper et al., 1988; Garrison and Kastner, 1990; Glenn, 1990; Arning et al., 2009a,b; Jaisi and Blake, 2010; Cosmidis et al., 2013; Bruggmann et al., 2022). More recently, researches also focused on Cenozoic Peruvian onshore basins (Gallarday, 2009; Bech et al., 2010; Zegarra and Canales, 2013; Castañeda and Rivera, 2016). The first record of Miocene Peruvian phosphate deposits was reported by Lisson (1898) precisely in the Ocucaje area (Ica Province) from the East Pisco Basin. Later, MacDonald (1956) and Cheney et al. (1979) described phosphorite deposits from the Sechura Basin. These phosphate deposits are marine in origin and mainly constituted by pellets formed by well-sorted sand-sized grains of fluorhydroxycarbonate apatite (Cheney et al., 1979). They lay on erosive basal surfaces cutting through the underlying diatomites (Cheney et al., 1979). In the forearc basins, the ODP Leg 112 coring campaign revealed the occurrence of phosphatic materials at six sites on the shelf and upper slope off Peru (Garrison and Kastner, 1990). Three different types of phosphates were recognized, namely, F-phosphates (i.e., friable, light-colored micronodules), D-phosphates (i.e., dark, dense phosphates), and P-phosphates (i.e., phosphatic sands) (Garrison, 1992). These sites recorded phosphate deposition starting from the Middle Miocene onward, with higher phosphate abundances being observed in the Pliocene and (especially) Quaternary sediments, which probably reflects the higher frequency of fluctuations of the physico-chemical conditions controlling phosphate formation during pronounced glacial/interglacial cycles. Onshore, in the East Pisco Basin, firstly Lisson (1898) and later Gallarday (2009) reported on the occurrence of phosphate deposits in the desert near Ocucaje, as also mentioned by Zegarra and Canales (2013). Gallarday (2009) provided petrographic and geochemical data on these deposits, which are described as characterized by terrigenous material and phosphate nodules with a P_2O_5 content around 17%. In addition, Castañeda and Rivera (2016) studied the microscopical and chemical composition of Miocene phosphorites from both the Pisco and Sechura basins. They classified these phosphorites in three main phosphatic facies based on an economic approach: thus, oolitic phosphorites are found in both the Pisco and Sechura basins, intraclastic phosphorite only occur in Sechura Basin, and phosphatic nodules and conglomerates are only found in the East Pisco Basin. Their studies suggest that the Pisco and Sechura phosphorites are similar in chemistry (e.g., by displaying a chlorine deficiency) and that apatite is diagenetically formed as a direct chemical precipitate. However, a comprehensive investigation aimed at understanding the processes and the sedimentological conditions that led to phosphogenesis and phosphorite accumulation in the East Pisco Basin is still lacking. This gap is addressed here by characterizing previously undocumented, laterally extensive layers of phosphorite deposits occurring in the Pisco Formation.

In the East Pisco Basin, the largely Miocene Pisco Formation is known for its exceptional paleontological content (e.g., Esperante et al., 2015; Bosio et al., 2021a; Bianucci and Collareta, 2022). The Pisco Formation consists of several unconformity-bounded units, at the base of which phosphorite deposits occur (Di Celma et al., 2017). These basal lags are characterized by pebble-to boulder-size lithic clasts, pebble-size phosphate nodules, cobble-size dolomitic clasts featuring bivalve borings, shark teeth, and bone fragments (Di Celma et al., 2017). Due to its well-defined stratigraphic, sedimentary and paleoenvironmental context, the East Pisco Basin is ideally suited for reconstructing the depositional regime and the chemical-physical conditions in which shallow-marine authigenic phosphates formed during early transgression. Unraveling the sedimentological processes involved in the phosphogenesis, as well as comprehending the sedimentological significance of the P-rich intervals, is of particular interest for understanding how phosphorites formed in the past as well as for supporting the exploration of these relevant resources, especially along the Peruvian coast.

2. Geological setting and basin stratigraphy

The Peruvian convergent margin is predominantly erosive rather than accretionary (e.g., Clift and Vannucchi, 2004; Noda, 2016). Its forearc basin system shows distinct cross-margin segmentation and is further divided by the Outer Shelf High, a northwest-trending structural high point of the Precambrian-Paleozoic basement. As a result, the system is organized into an inner and an outer series of elongated, trench-parallel basins (Thornburg and Kulm, 1981; Kulm et al., 1982) (Fig. 1a). Nowadays, the forearc region immediately landward of where the aseismic Nazca Ridge impinges on the continental margin comprises the onshore inner East Pisco Basin (EPB) and the poorly known offshore West Pisco Basin (WPB). These two basins are separated from each other by the uplifted Coastal Cordillera structural high, which represents the subaerial prolongation of the Outer Shelf High (Romero et al., 2013). The subsidence and uplift history of this pair of forearc basins reflects the dynamic interaction between the subducting and overriding plates along the Peruvian convergent margin (von Huene and Suess, 1988; Herbozo et al., 2020), thus revealing several stages of deformation at varying temporal and spatial scales (e.g., Viveen and Schlunegger, 2018).

The stratigraphy of the sedimentary fill of the EPB comprises two tectonostratigraphic packages, namely, the P and N megasequences, which are separated by a regionally traceable unconformity marking a major phase of basin development (Di Celma et al., 2022). The sedimentation on the basement began at least during middle Eocene times (Coletti et al., 2019; Malinverno et al., 2021) and continued in the late Eocene and early Oligocene with the deposition of the Paracas and Otuma formations of the P megasequence. During this time interval, a single forearc Pisco basin existed; its configuration changed during the (late?) Oligocene, when the basin underwent a prolonged period of subaerial exposure and its central part was uplifted to form the trench-parallel, normal-fault-bounded Coastal Cordillera structural high, thus giving birth to the double forearc basin comprising the EPB and the WPB (Di Celma et al., 2022). By the earliest Miocene, basal subduction erosion and thinning of the overriding plate resulted in

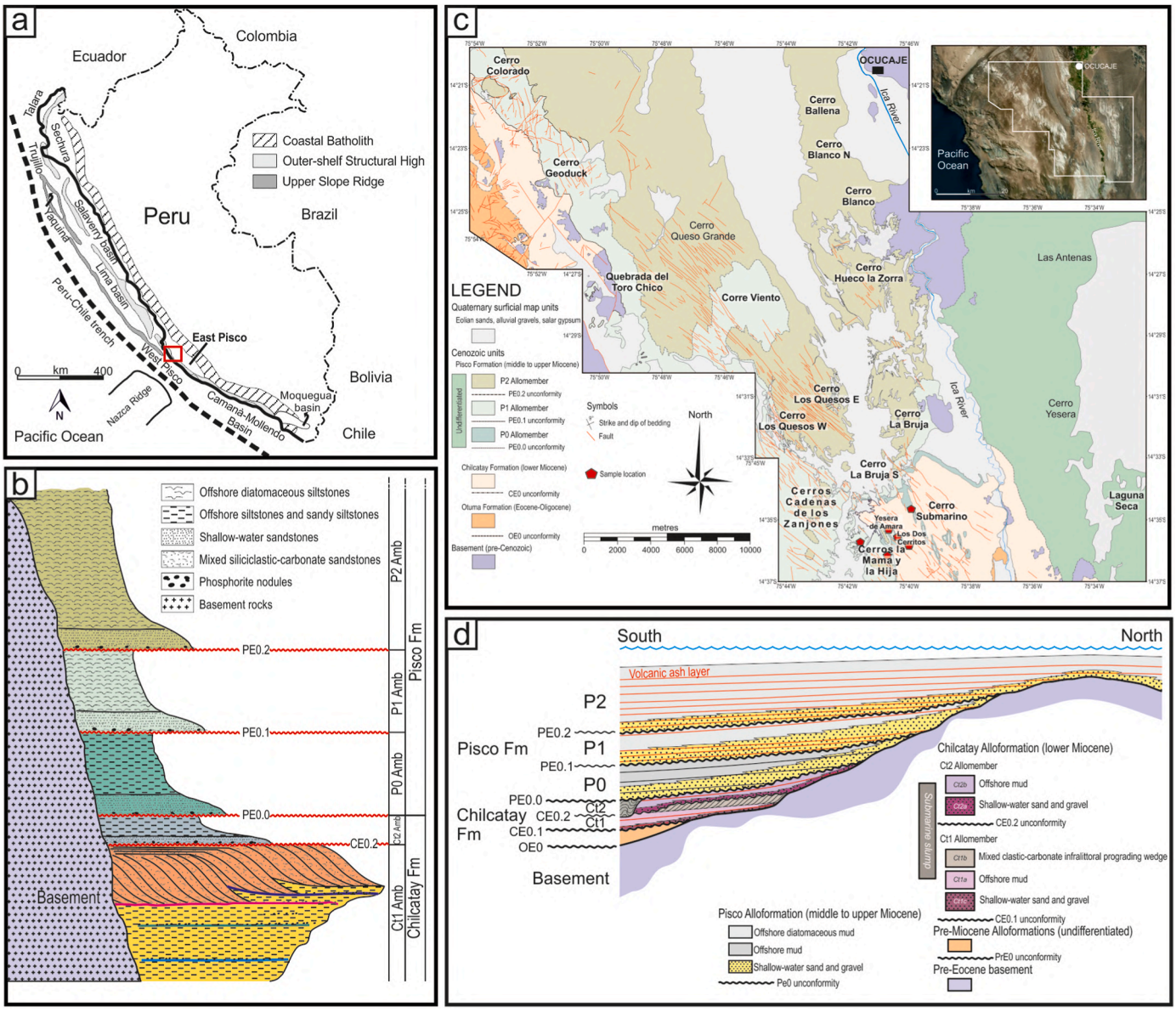

Fig. 1. Geographic and geological framework. **a)** Location of the East Pisco Basin along the Peruvian coast; **b)** Stratigraphy of the Pisco Formation (P0, P1, P2) on top of the Chilcatay Formation (modified after Di Celma et al., 2018a); **c)** Simplified geological map of the exposures of the Pisco Formation investigated in the Ocucaje area (modified after Bosio et al., 2021a) and sampling locations; **d)** Stratigraphic scheme of the East Pisco Basin fill along the Ica River with the stratigraphic position of the volcanic ash layers (modified after Di Celma et al. (2019).

renewed subsidence and marine transgression over the basin (Clift and Hartley, 2007; Herbozo et al., 2020). As such, marine sedimentation resumed in the present-day EPB with the deposition of the Lower Miocene Chilcatay Formation and the Middle to uppermost Miocene, or possibly Pliocene, Pisco Formation of the N megasequence.

Stratigraphic analyses of the Chilcatay and Pisco sediments exposed astride the Ica River valley revealed multiple internal stratal surfaces that led to the identification of three high-order sequences both in the Chilcatay Formation (namely, Ct0, Ct1 and Ct2; Di Celma et al., 2018b, 2019; DeVries et al., 2021; Bosio et al., 2022) and in the Pisco Formation (namely, P0, P1 and P2; Di Celma et al., 2016a, b, 2017, 2018a; Collareta et al., 2021a) (Fig. 1b–d). The oldest sequence in the Chilcatay Formation (Ct0) spans the earliest Miocene, between ca. 22 Ma and 20 Ma (DeVries et al., 2021; Bosio et al., 2022), whereas the Ct1 and Ct2 strata date back to between 19.2 and 18.0 Ma, with the age of the base of Ct2 being constrained between 18.4 and 18.1 Ma (Bianucci et al., 2018; Di Celma et al., 2018b; Lambert et al., 2018; Bosio et al., 2020b, 2020c, 2022). In the study area, the deposition of P0 and P1 took place between 14.7–12.6 Ma and 9.5–8.6 Ma, respectively, whereas the age of P2 is constrained to 8.4 and $\geq$ 6.71 Ma (Gariboldi et al., 2017; Bosio et al., 2020b, 2020c, 2022).

In the Pisco Formation, the bounding unconformities at the base of P0, P1 and P2 have been named PE0.0, PE0.1 and PE0.2, respectively (Fig. 1c and d). These surfaces record abrupt seaward shifts in facies and are commonly demarcated by a *Glossifungites* Ichnofacies dominated by *Thalassinoides* excavated into a semiconsolidated (firmground) substrate and *Gastrochaenolites* borings in a hardground substrate (Di Celma et al., 2017). The overlying strata were deposited within a lower shoreface to offshore setting, being arranged in a deepening-upward, transgressive trend in which downdip facies associations step up over updip facies associations (Di Celma et al., 2022). In particular, the bounding discontinuities are covered by coarse-grained transgressive lags up to 0.4 m thick. These lags are overlain by moderately to highly bioturbated, sand-rich lower shoreface units that transition into either offshore

massive siltstones in P0 or gray-white diatomaceous mudstones featuring subordinate amounts of volcanic ash layers, thin sandstone beds and dolomitized mudstone horizons in P1 and P2. Phosphorite layers can be observed not only in the Pisco Formation but also along the older unconformities of the EPB, such as the three basal unconformities of the Ct0, Ct1 and Ct2 sequences of the Chilcatay Formation (namely, CE0.0, CE0.1 and CE0.2) (Di Celma et al., 2022).

3. Analytical methods

Phosphorite bulk samples were collected from the basal lags of the three sequences of the Pisco Formation at the localities of Cerro Submarino, Cerro Yesera de Amara, Los dos Cerritos, Cerros la Mama y la Hija, and an as-yet unnamed small hill located just north of Cerro la Mama y la Hija (14°35′47.50"S - 75°41′32.40"W), which is informally referred to herein as Cerro Innominado (see Table 1; Fig. 1c). Ten samples were subjected to different petrographic and geochemical analyses. They were selected to be representative of the lateral variability observed macroscopically in the field at different localities (Table 1). Following a first macroscopic description and selection aimed at representing the facies variability, bulk samples were crushed and milled in agate jars, and subsequently prepared for mineralogical and geochemical analysis. Mineralogical analyses were performed by means of X-Ray Diffraction (XRD) through an X'Pert PRO PANalytical Diffractometer in parafocalizing Bragg-Brentano θ-θ geometry with a Spinner PW3064 sample holder at the Università degli Studi di Milano-Bicocca under the same analytical conditions as described in Malinverno et al. (2023). Major element chemical composition analyses were carried out via X-Ray Fluorescence (XRF) with an ARL 9400 XP + Sequential X-Ray Fluorescence Spectrometer at the Università di Pisa. Loss on Ignition (LOI) was determined at 950 °C. Trace element analysis was performed by means of Inductively Coupled Plasma-Mass Spectrometry (ICP-MS) on bulk samples with a PerkinElmer NexION 300x Spectrometer at the Università di Pisa. About 50–60 mg of each powdered sample was dissolved in a mixture of HF and HNO_3 on a hot plate at ~170 °C in a screw-top perfluoroalkoxy (PFA) vessel. Ultrapure Milli-Q water was used for diluting the solution. A procedural blank and 3 references samples underwent the same procedure. The geochemical references materials RGM-1 (Rhyolite Glass Mountain) (Govindaraju, 1994) and WS-E (Whin Sill Dolerite) (Govindaraju, 1994) were used to verify the accuracy of the analysis, whereas BE-N (alkali basalt) (Govindaraju, 1980) was used to calibrate the equipment. A solution containing ^{103}Rh, ^{187}Re and ^{209}Bi was added to the unknown, blank and reference samples as the internal standard.

Phosphorite samples were sub-sampled for performing petrographic and microanalytical investigations. Following the selection of the most representative samples, 9 polished thin sections of different types of components were prepared in the laboratories of TS Lab & Geoservices in Pisa. Thin sections were observed through the Nikon Eclipse LV 100N POL and BK-POL optical polarizing microscopes at the Università degli Studi di Milano-Bicocca in both transmitted and reflected light for describing the texture of the layers, the internal structure of the phosphate nodules, and the petrography of all the components.

Four thin sections representative of the occurrences of phosphate minerals were then carbon-coated for Scanning Electron Microscopy (SEM) and Energy-Dispersive X-ray Spectroscopy (EDS), and subsequently studied using a Zeiss FEG Gemini 500 at the Microscope Lab Facility of the Università degli Studi di Milano-Bicocca. Semi-quantitative EDS analyses (10 kV, working distance 7 mm) were performed on selected spots. These analyses allowed for investigating the fine structure of the components of the phosphorite layers, as well as the characterization of the diagenetic cements. In order to obtain quantitative chemical data on the phosphate minerals, Electron Probe Micro-Analysis (EPMA) was performed at the Dipartimento di Scienze della Terra "Ardito Desio", Università di Milano, using a JEOL JXA-8200 SuperProbe, with operating conditions of 15 kV, a beam current of 5 nA, and a beam diameter of 3 μm. Halogens were analyzed first. The EPMA instrument is equipped with five wavelength-dispersive spectrometers (WDS) with a range of LiF, PET and TAP crystals, and one additional EDS detector. The instrument was internally calibrated using mineral standards and metals of natural and synthetic origin, including: grossular (Si Kα, Ca Kα, Al Kα); omphacite (Na Kα); forsterite (Mg Kα); fayalite (Fe Kα); ilmenite (Ti Kα); orthoclase (K Kα); rhodonite (Mn Kα); pure metal Cr (Cr Kα); apatite (P Kα); hornblende (F Kα); scapolite (Cl Kα); and celestine (S Kα). Raw element data were ZAF-corrected using a phi-rho-Z analysis program, and corrected element contents were converted to oxide contents in weight percent (wt%) assuming stoichiometry.

Laser Ablation-Inductively Coupled Plasma-Mass Spectrometry (LA-ICP-MS) was carried out through an Analyte Excite 193 nm ArF excimer laser microprobe system equipped with an HelEx II volume sample chamber (Teledyne Photon Machines), coupled with a single-collector quadrupole ICP-MS (iCAP RQ; Thermo-Fisher Scientific) at the Geochemistry, Geochronology and Isotope Geology laboratory of the Dipartimento di Scienze della Terra "Ardito Desio", Università di Milano. The NIST SRM 612 synthetic glass and ^{43}Ca measured with EPMA were used as external and internal standards, respectively. Quality control of the analyses was achieved by analyzing the USGS reference basalt glass BCR-2G together with the unknown. Precision was better than 5% and accuracy was within 2σ. A laser fluence of 2 J/cm^2 and a repetition rate of 10 Hz were set for the unknown. The laser spot size was set to 50 μm, to minimize the limits of detection. The He flow rate was set to 0.5 L/min in the sample chamber and to 0.25 L/min in the HelEx II cup. Each analysis consisted of the acquisition of 40 s of background signal, about 60 s of laser signal, and 20 s of wash-out time.

4. Results

4.1. Field data

Phosphorite layers in the Pisco Formation were observed from several localities in the Ica River area. From north-west to south-east, they were identified at Cerro Colorado, Cerro Los Quesos, Cerro Cadena de los Zanjones, Ullujaya, Cerro Submarino, Cerro Yesera de Amara, Los dos Cerritos, Cerros la Mama y la Hija and Cerro Innominado

Table 1
List of the analyzed samples with sample localities, corresponding unconformities and type of analyses.

Samples	Locality	Unconformity	OM	XRD	XRF	SEM	EPMA	ICP-MS	LA-ICP-MS
SUB-1	Cerro Submarino	PE0.0	X	X	X	X	X	X	X
SUB-1-bis	Cerro Submarino	PE0.0	X						
YA-SOT	Cerro Yesera de Amara	PE0.1	X	X		X			
YADA-F1	Cerro Yesera de Amara	PE0.0	X						
YADA-F2	Cerro Yesera de Amara	PE0.1	X				X		X
IN-F3	Cerro Innominado	PE0.2	X	X					
FOSF-1a	Los Dos Cerritos	PE0.0			X			X	
FOSF-1b	Los Dos Cerritos	PE0.0			X			X	
MH-3	Cerros la Mama y la Hija	PE0.2			X			X	
MH-6	Cerros la Mama y la Hija	PE0.2	X			X	X		X

(see Fig. 1c). They overlie the unconformity surfaces at the base of each sequence of the Pisco Formation, namely PE0.0, PE0.1 and PE0.2 (Fig. 1c and d).

In the field, phosphorite layers display a patchy distribution, with variable thicknesses and content. They range in thickness from a few cm up to ca. 40 cm, and are usually poorly sorted, clast-supported, and devoid of any appreciable vertical grading (Fig. 2a–f). The components, which consist of reworked and autochthonous early diagenetic products, are set in a scarce, poorly cemented sandy matrix and include granule-to pebble-sized phosphate clasts (Fig. 2a–c), cobble-sized dolomite clasts displaying bivalve borings (*Gastrochaenolites*) (Fig. 2d), dolomite internal molds of gastropods and articulated bivalves (Fig. 2e), shark teeth (Fig. 2e), polished marine vertebrate bone fragments, and partially articulated skeletal elements of marine mammals. Phosphate clasts are brownish in color and range in shape from subrounded to well-rounded, with a low to high sphericity. They can be mixed with pebble-to large boulder-sized igneous clasts, whose occurrence represents the most common lithological expression of the sequence boundaries in the EPB (e.g., Di Celma et al., 2018a: Fig. 3a).

Phosphorites typically lay on a sharp, irregular surface demarcated by a *Glossifungites* Ichnofacies burrowed into the underlying diatomite-siltstone firmground. This ichnofacies is generally comprised of common *Thalassinoides* (Fig. 2c) and *Gyrolithes*; *Gastrochaenolites* traces are also present, being typically developed on both sides of large dolomite clasts (Fig. 2d).

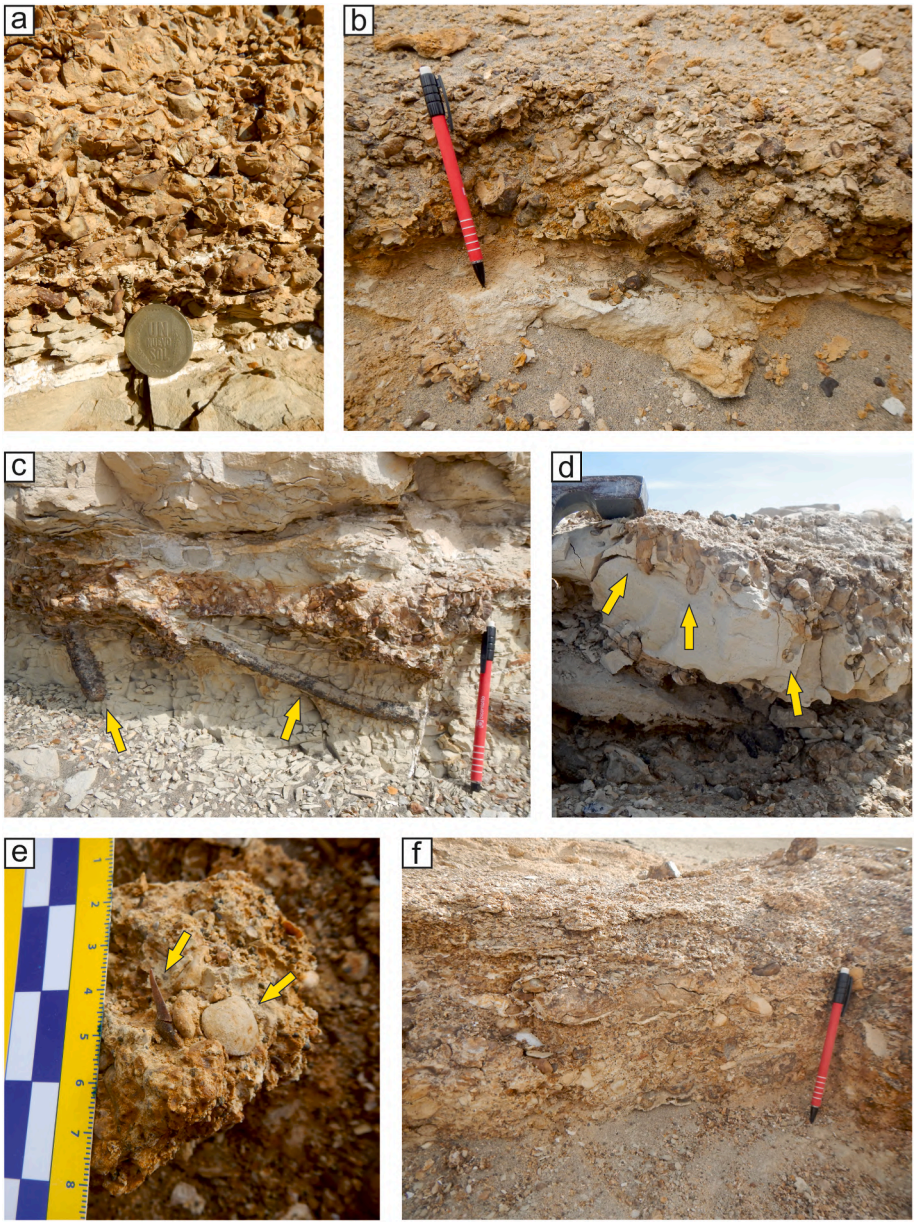

Fig. 2. Field outcrops of phosphorite layers from different unconformity surfaces, showing details of the facies variations. **a)** Detailed view of closely-packed phosphate granules and pebbles in dolomitized matrix laying on siltite - PE0.0 at Ullujaya; **b)** 20-cm thick layer of phosphate pebbles in dolomitized matrix lying on diatomite - PE0.0 at Los dos Cerritos; **c)** 5–10 cm thick layer of phosphate pebbles and phosphate filling of *Thalassinodes* burrows (yellow arrows) into underlying diatomite firmground - PE0.1 at Cerro Yesera de Amara; **d)** detail of decimetric-sized diatomite hardground pebble with *Trypanites* ichnofacies (yellow arrows) on both sides and phosphorite filling the perforations - PE0.2 at Cerro Colorado; **e)** detail of phosphate granules-pebbles with mollusk dolomite molds and a shark tooth (yellow arrows) - PE0.2 at Cerro Innominado; **f)** 25 cm thick layer of phosphate granules and pebbles with dolomite clasts - PE0.2 at Cerro Innominado.

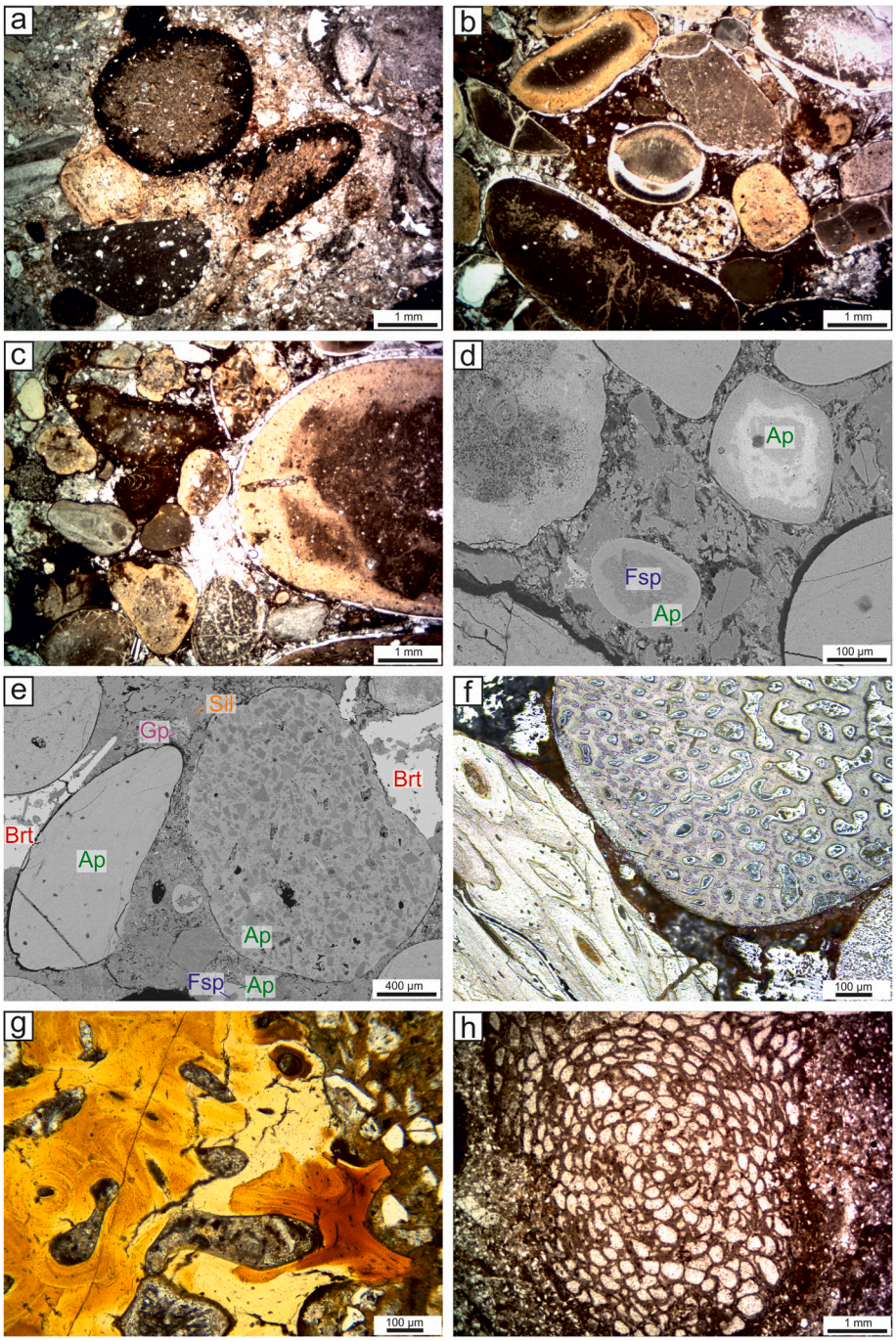

Fig. 3. Photomicrographs and SEM images of the phosphorite layer components. **a)** Poorly sorted, subrounded to well-rounded phosphatic and dolomite clasts showing a low to high sphericity, and a rounded bone fragment under transmitted plane-polarized light. Sample SUB-1-bis at the base of the P0 sequence at Cerro Submarino. **b)** Poorly sorted, subrounded to well-rounded phosphatic and dolomite clasts showing a low to high sphericity and a probable tooth fragment under transmitted plane-polarized light. Sample MH-6 at the base of the P2 sequence at Cerros la Mama y la Hija. **c)** Poorly sorted, subrounded to well-rounded phosphatic and dolomite clasts showing a low to high sphericity under transmitted plane-polarized light. Sample MH-6 at the base of the P2 sequence at Cerros la Mama y la Hija. **d)** BSE image of phosphatic clasts composed of detrital minerals and foraminifera cemented by fluorapatite, and small nodules with a phosphate and a feldspar crystal in the core. Sample MH-6 at the base of the P2 sequence at Cerros la Mama y la Hija. **e)** BSE image of phosphatic clasts composed of detrital minerals cemented by fluorapatite, well-rounded bone fragments and small nodules with a feldspar crystal in the core. Cements are composed of silica, gypsum and baryte. Sample MH-6 at the base of the P2 sequence at Cerros la Mama y la Hija. **f)** Rounded bone fragments of marine vertebrates exhibiting compact and cancellous bone tissues under reflected light. Sample MH-6 at the base of the P2 sequence at Cerros la Mama y la Hija. **g)** Marine vertebrate bone fragment with the typical reddish color due to Fe-oxyhydroxides under transmitted plane-polarized light. Sample YADA-F1 at the base of P0 sequence at Cerro Yesera de Amara. **h)** Bryozoan specimen under transmitted plane-polarized light. Sample YA-SOT at the base of the P1 sequence at Cerro Yasera de Amara. Mineral abbreviations following Whitney and Evans (2010).

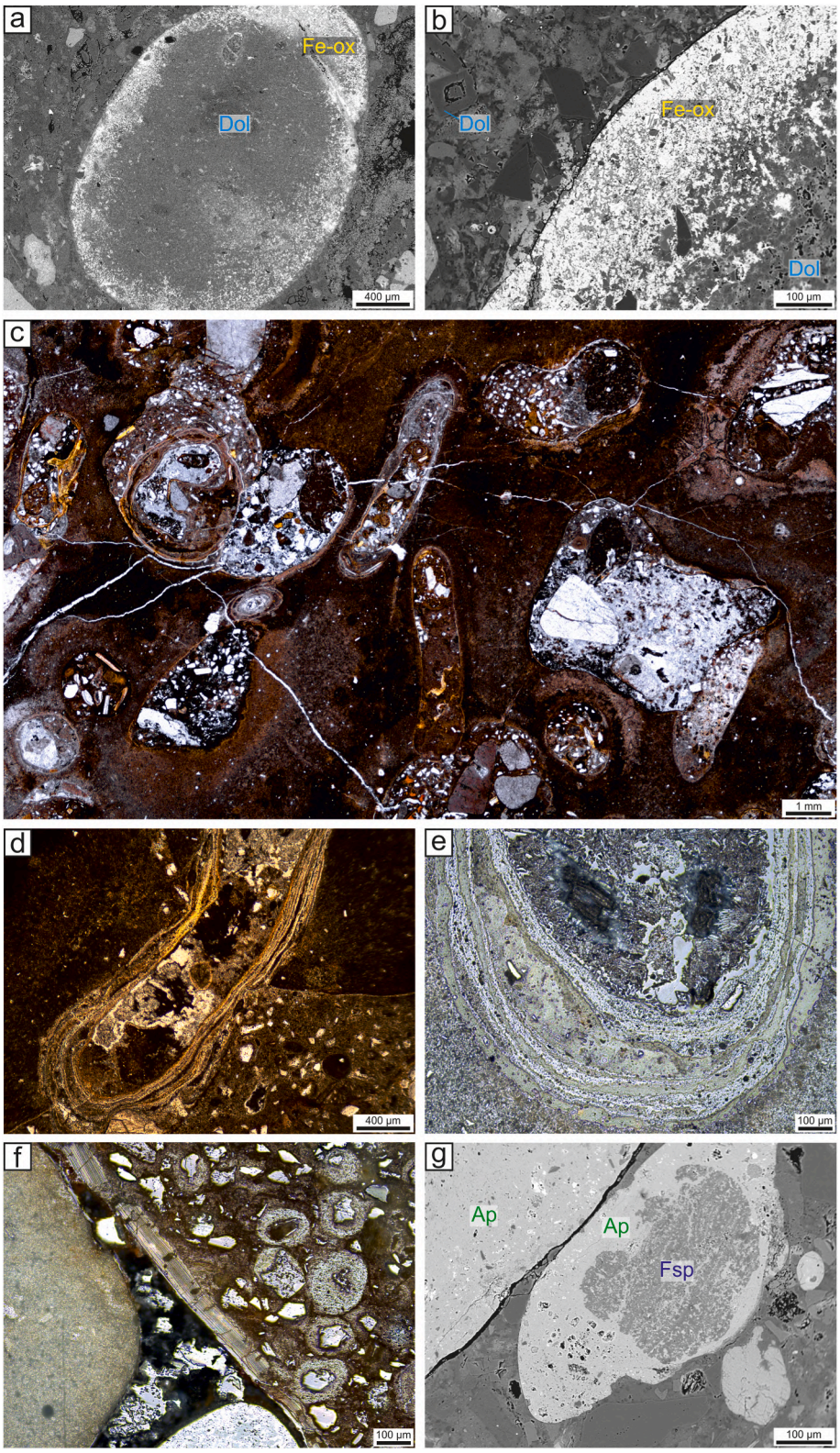

Fig. 4. Photomicrographs and SEM images of the phosphorite layer components. **a)** BSE image of a dolomite-cemented clast that exhibits a Fe-oxyhydroxide coating. Sample SUB-1 at the base of the P0 sequence at Cerro Submarino. **b)** Close-up of a dolomite-cemented clast that exhibits a Fe-oxyhydroxide coating (BSE image). Note the rhombohedral dolomite crystal. Sample SUB-1 at the base of the P0 sequence at Cerro Submarino. **c)** A phosphatic clast under transmitted plane-polarized light, exhibiting burrows with phosphatic laminites similar to those described by Berndmeyer et al. (2012). Sample IN-F3 at the base of the P2 sequence at Cerro Innominado. **d)** Close-up of one burrow in the phosphate clast under transmitted plane-polarized light. Sample IN-F3 at the base of the P2 sequence at Cerro Innominado. **e)** Close-up of a laminite in a burrow under reflected light. Sample IN-F3 at the base of the P2 sequence at Cerro Innominado. **f)** Small nodules with single crystals at the core and a fluorapatite coating forming a bigger phosphatic clast under reflected light. Sample MH-6 at the base of the P2 sequence at Cerros la Mama y la Hija. **g)** BSE image of a phosphate nodule with a feldspar at the core and a fluorapatite coating. Sample SUB-1 at the base of the P0 sequence at Cerro Submarino. Mineral abbreviations following Whitney and Evans (2010).

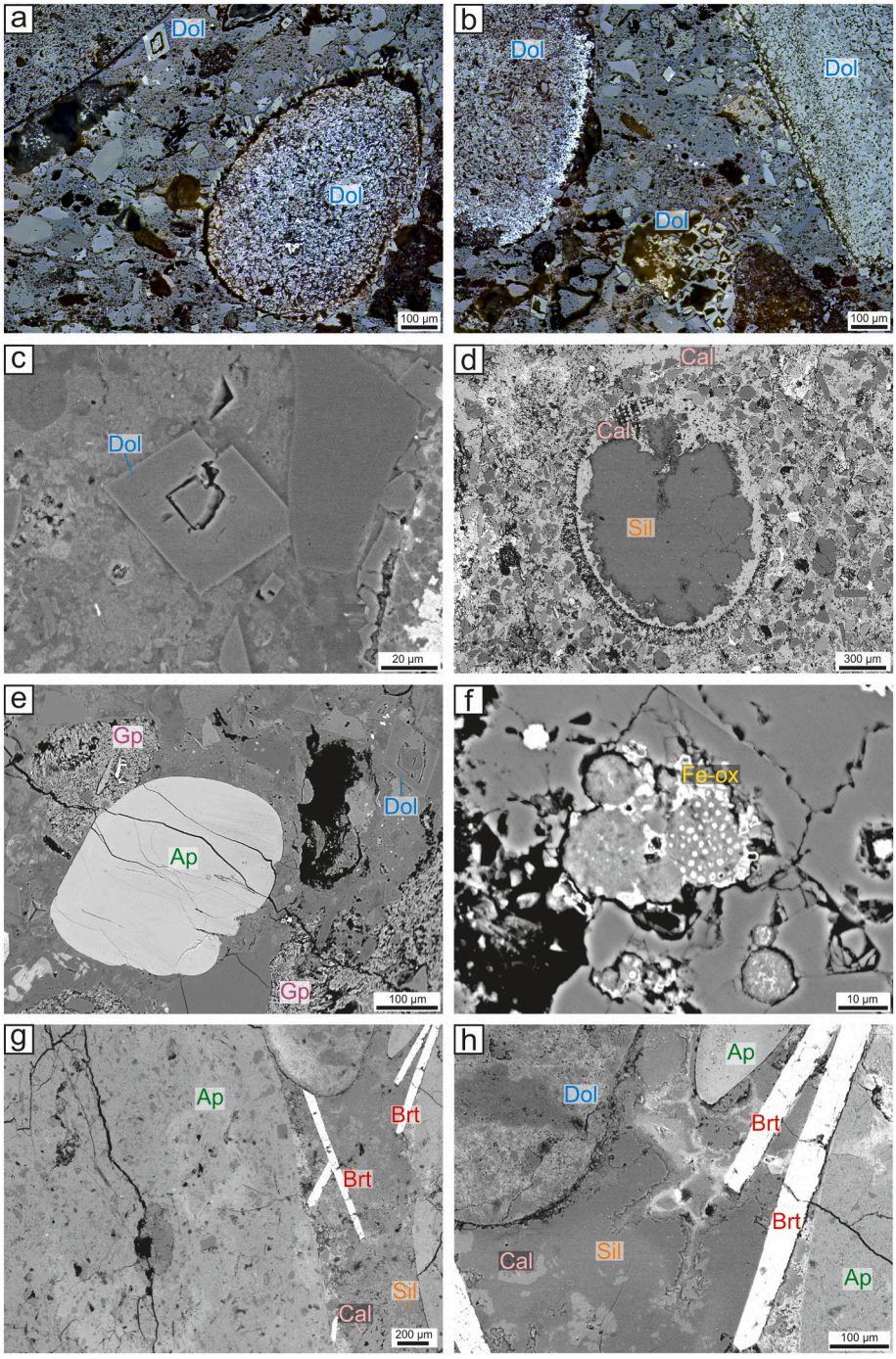

Fig. 5. Photomicrographs and SEM images of the phosphorite layer cements. **a)** Dolomite clasts in dolomite cement with rhombohedral crystals under reflected light. Sample SUB-1 at the base of the P0 sequence at Cerro Submarino. **b)** Dolomite clasts in dolomite cement with rhombohedral crystals under reflected light. Sample SUB-1 at the base of the P0 sequence at Cerro Submarino. **c)** BSE image of a rhombohedral dolomite crystal. Sample SUB-1 at the base of the P0 sequence at Cerro Submarino. **d)** BSE image of an echinoderm spine substituted by silica cement in a calcite cemented surrounding sediment. Sample YA-SOT at the base of the P1 sequence at Cerro Yesera de Amara. **e)** BSE image of a fluorapatite fragment in a mixed gypsum and dolomite cement. Note the big rhombohedral dolomite crystal. Sample SUB-1 at the base of the P0 sequence at Cerro Submarino. **f)** BSE image of a close-up of a framboidal Fe-oxyhydroxide, ghost of a pyrite framboid, in the dolomite cement. Sample YA-SOT at the base of the P1 sequence at Cerro Yesera de Amara. **g)** BSE image of baryte crystals in a silica and calcite cement surrounding phosphatic clasts. Sample MH-6 at the base of the P2 sequence at Cerros la Mama y la Hija. **h)** BSE image of baryte crystals in a silica and calcite cement surrounding phosphate- and dolomite-cemented clasts. Sample MH-6 at the base of the P2 sequence at Cerros la Mama y la Hija. Abbreviations following Whitney and Evans (2010).

4.2. Mineralogy and petrography

The component clasts of the phosphorite layers are tens of micrometers to few centimeters in diameter, with a subrounded to well-rounded morphology and a low to high sphericity (Fig. 3a–c). They can be differentiated into two main types: phosphatic clasts (mainly consisting of Ca-phosphate minerals) and dolomite-cemented clasts (Fig. 3a–e, 4a, b). Both types may host detrital minerals (e.g., feldspar, quartz) and rare fossil shells, such as foraminifera and diatoms (Fig. 3d and e). Bone fragments are usually common in these layers and look

Table 2
XRD results showing the main mineral phases. Sample SUB-1-bis from PE0.0 at Cerro Submarino; sample YA-SOT: from PE0.1 at Cerro Yasera de Amara; sample IN-F3 from PE0.2 at Cerro Innominado. Values are reported in wt%.

Stratigraphic position	PE0.0	PE0.1	PE0.2
Sample	SUB-1	YA-SOT	IN-F3
quartz	25.3	8.5	5.0
plagioclase	17.1	27.6	19.8
dolomite	13.5	10.9	6.9
hydroxyapatite/fluorapatite	13.3	3.9	10.9
calcite	12.1	18.8	49.5
gypsum	11.1	17.4	7.9
stilbite	7.6	4.7	–
montmorillonite	–	4.4	–
illite/muscovite	–	3.8	–

polished (Fig. 3f and g), which suggests some degree of mechanical abrasion. In one sample, YA-SOT, encrusting bryozoan remains were also found within the phosphatic layer at the base of the P1 sequence at Cerro Yesera de Amara (Fig. 3h).

Clasts often exhibit a thin Fe-oxyhydroxide coating that is clearly visible in SEM-BSE images as a bright rim (Fig. 4a and b). In one case (sample IN-F3 from the base of the P2 sequence at Cerro Innominado), phosphatic clasts show burrows coated by laminites (Fig. 4c–e) as described by Arning et al. (2009a) in the recent Peruvian phosphorites. They can also exhibit bioerosion in the form of borings.

Small phosphatic nodules are common. They include a core made of a single particle (such as feldspar or quartz) or bone fragment, and a phosphatic coating made of concentric layers (Fig. 4f and g), similar to the redox-aggregated grains (RA grains) described by Pufahl and Grimm (2003). In one case, these small nodules are part of a bigger phosphatic clast coated by phosphatic laminite (Fig. 4f).

Phosphatic and dolomite clasts, small nodules and bone fragments are bound together by different types of cements, namely dolomite, silica, calcite and gypsum/anhydrite (Fig. 5). Large rhombohedral crystals of dolomite are commonly distributed in the cemented phosphorite layers (Fig. 5a–c). Besides of dolomite, the main cements are silica and calcite, usually found together (Fig. 5d–g, h). Along the edges of clasts and filling voids, gypsum/anhydrite crystals also occur (Fig. 5e). Framboidal Fe-oxyhydroxides, usually coating phosphate- and/or dolomite-cemented clasts, are also found scattered within the cement (Fig. 5f). In addition, baryte is present in the form of both pervasive cement and big euhedral crystals (Fig. 5g and h).

XRD results of three analyzed samples representing the three phosphorite layers above the PE0.0, PE0.1 and PE0.2 unconformities, respectively, indicate a similar mineralogical composition, with variable proportions of the components (see Table 2). Plagioclase and quartz represent the main detrital components of the layer, ranging in abundance between 17.1–27.6 wt% and 5.0–25.3 wt%, respectively (Table 2). Calcite, occurring both as fossil shell fragments and cement, displays high abundance variations (from 12.1 to 49.5 wt%) (Table 2). Dolomite ranges between 6.9 and 13.5 wt%, whereas the Ca-phosphate minerals (hydroxyapatite/fluorapatite) range from 3.9 to 13.3 wt% (including the apatite cement and bone fragments) (Table 2). Ca-sulfate minerals are represented by gypsum, which is present in all the samples, with abundance ranging between 7.9 and 17.4 wt% (Table 2). Other less abundant minerals include zeolites (stilbite) and phyllosilicates (montmorillonite and illite/muscovite) (Table 2).

4.3. Geochemistry

4.3.1. Bulk rock geochemistry

The major element chemical composition of the phosphatic beds can be presented in terms of the wt% proportions between the components P_2O_5+CaO + Na_2O, SiO_2+Al_2O_3+K_2O and Fe_2O_3+MgO (Fig. 6a). Our chemical data are in overall agreement with previously published ones from the same region (Castañeda and Rivera, 2016), although the samples from the present work are relatively poorer in SiO_2+Al_2O_3+K_2O compared with most previous analyses, which may indicate a lesser abundance of terrigenous materials. In more detail, silica content is ca. 23 to 25 wt%, with a minimum value of ca. 14 wt% for sample SUB-1 (Table 3). CaO and P_2O_5 contents range between 26 and 36 wt% and between 3 and 10 wt%, respectively. Iron content, reported as Fe_2O_3tot, is around 4 wt% in all samples. The LOI (Loss On Ignition) is about 25–26% in all the samples, except for the MH-3 sample where it is 12%. For what concerns the CaO/P_2O_5 ratio, the ratio is around 3 for the phosphatic layer at the base of P2, while that at the base of P0 displays a higher CaO/P_2O_5 ratio (Table 3). The high value of the CaO/P_2O_5 ratio and the correlation between CaO and Sr suggests that the CaO content is due to the presence of carbonates (calcite and dolomite), as e.g. in cements.

4.3.2. In situ major and minor element analysis

The major element composition of phosphate minerals determined by EPMA microanalysis on phosphatic clasts and nodules plots towards

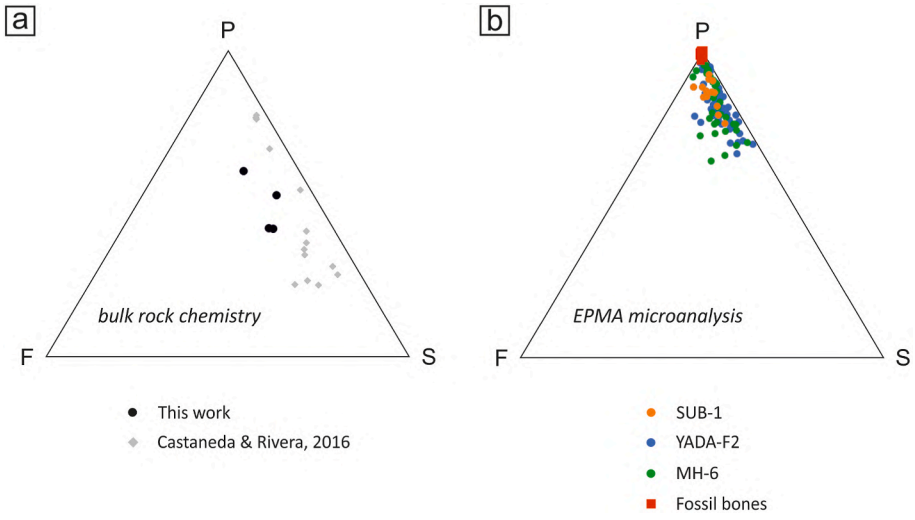

Fig. 6. Chemical composition of phosphorite beds in ternary diagrams with apexes P (P_2O_5+CaO+Na_2O) – S (SiO_2+Al_2O_3+K_2O) – F (Fe_2O_3+MgO). **a)** Bulk rock composition of the Pisco phosphorites analyzed in this work, compared with previous data. **b)** EPMA chemical composition of the Ca-phosphate in phosphatic clasts and bone fragments in the Pisco phosphorites (data from this work).

Table 3
XRF analyses of four phosphorite samples. SUB-1 is from PE0.0 at Cerro Submarino. FOSF-1 is from PE0.0 at Cerro Submarino. MH-3 is from PE0.2 at Cerros la Mama y la Hija. Values are reported in wt%. L.O.I. = Loss On Ignition.

Stratigraphic position	PE0.0	PE0.0	PE0.0	PE0.2
Sample	SUB-1	FOSF-1a	FOSF-1b	MH-3
SiO_2	13.62	23.37	24.52	25.29
TiO_2	0.30	0.30	0.24	0.38
Al_2O_3	3.09	4.94	5.19	5.67
Fe_2O_3	4.57	3.92	4.00	3.91
MnO	0.14	0.14	0.14	0.21
MgO	6.90	9.27	8.52	5.10
CaO	36.42	26.16	26.00	31.88
Na_2O	1.73	1.47	1.61	3.94
K_2O	0.51	0.92	0.92	0.89
P_2O_5	6.73	3.41	3.65	10.30
sum	74.01	73.90	74.79	87.57
L.O.I.	25.99	26.10	25.21	12.43

the P-apex of the P_2O_5+CaO+Na_2O vs SiO_2+Al_2O_3+K_2O vs Fe_2O_3+MgO diagram (Fig. 6b). While the fossil bone fragments composition plots right on the P apex, the phosphatic clasts may contain up to about 20% of SiO_2+Al_2O_3+K_2O. Similar results were found for recent Peruvian phosphorites by Glenn and Arthur (1988), who suggested abundant submicrometric terrigenous mineral inclusions, which could not be excluded during the analysis. This is also made evident by the very variable silica content as resulting from the EPMA analysis (Table 4; see Supplementary Table S1 for the entire dataset).

The composition of the phosphate corresponds to fluorapatite, with an average CaO content of about 41–47 wt%, an average P_2O_5 content of ca. 27 wt% and an average F content of 3 wt% in the three phosphatic layers (Table 3). Analyses on fossil bones reveal an average CaO content of about 51–53 wt%, an average P_2O_5 content between 25 and 28 wt% and an average F content of 3–4 wt% (Table 3), similar to the "type 3b" bones of Bosio et al. (2021c), i.e., bones that have been subjected to a prolonged apatite recrystallization, resulting in a dark amber color and a moderate hardness.

4.3.3. Rare earth element composition and redox-sensitive elements

The ΣREE content of the Pisco phosphorite layers is low, being 41–65 ppm for the bulk rock analysis, while the LREE/HREE ratios are poorly variable, with La/Yb around 11 for the bulk rock analysis (Table 5).

Table 5
Trace element chemical composition of phosphorite bulk samples, obtained by means of ICP-MS.

Stratigraphic position	PE0.0	PE0.0	PE0.0	PE0.2
Sample	SUB-1	FOSF-1a	FOSF-1b	MH-3
Li	7.71	12.51	12.57	15.11
Be	0.72	1.03	1.02	1.36
V	74.84	92.55	92.46	75.61
Cr	44.82	62.86	60.54	48.76
Co	4.19	3.27	3.14	6.76
Ni	39.96	26.31	26.06	31.51
Cu	13.69	11.91	12.94	21.53
Zn	19.46	48.15	51.09	55.09
Ga	3.56	5.03	4.91	6.34
Rb	23.36	35.66	35.29	34.83
Sr	1002	687	675	925
Y	17.15	18.52	18.72	21.91
Zr	29.60	41.43	40.50	52.51
Nb	2.14	3.03	2.89	4.25
Mo	16.81	12.38	12.07	35.42
Cs	1.35	1.88	1.84	1.76
Ba	143	2762	2476	242
La	10.19	13.57	12.87	13.77
Ce	15.20	22.24	21.09	25.01
Pr	1.78	2.71	2.61	3.05
Nd	6.92	10.46	10.13	11.68
Sm	1.31	1.99	1.95	2.21
Eu	0.32	0.54	0.53	0.55
Gd	1.46	2.05	2.07	2.27
Tb	0.22	0.29	0.31	0.35
Dy	1.45	1.86	1.93	2.15
Ho	0.34	0.41	0.43	0.47
Er	1.05	1.27	1.31	1.46
Tm	0.16	0.18	0.19	0.21
Yb	0.95	1.17	1.20	1.27
Lu	0.16	0.19	0.19	0.21
Hf	0.66	1.01	1.01	1.12
Ta	0.16	0.22	0.21	0.30
Pb	8.86	5.22	5.25	7.56
Th	2.60	3.81	3.72	4.24
U	61.53	35.32	32.74	52.16
Sc	4.47	6.21	6.40	7.09

The content of redox-sensitive elements is also rather constant, with U contents of 33–62 ppm, Cu contents of 12–22 ppm, and Ni contents of 26–40 ppm (Table 5). The Ba content is high and variable (140–2800 ppm), probably due to the variable presence of late baryte. Sr

Table 4
Mean, number of analyses (in brackets) and standard deviation (SD) of the Electron Probe Microanalysis (EPMA) of the phosphorite clasts and bones of the samples YADA-F2, SUB-1 and MH-6 from the phosphorite layers at Cerro Yesera de Amara, Cerro Submarino and Cerros la Mama y la Hija, respectively. Values are reported in wt%.

	PE0.1		PE0.1		PE0.0		PE0.0		PE0.2		PE0.2	
	YADA-F2		YADA-F2 bones		SUB-1		SUB-1 bones		MH-6		MH-6 bones	
	Mean [58]	SD	Mean [4]	SD	Mean [13]	SD	Mean [8]	SD	Mean [39]	SD	Mean [8]	SD
SiO_2	13.40	11.35	0.03	0.02	6.76	2.93	0.10	0.09	7.95	5.52	0.43	0.45
TiO_2	0.23	0.69	0.01	0.02	0.41	0.98	0.02	0.03	0.12	0.19	0.02	0.02
Al_2O_3	3.60	2.22	0.02	0.01	1.03	0.58	0.01	0.01	1.92	1.45	0.05	0.02
FeO	3.06	3.73	0.14	0.02	3.13	1.53	0.23	0.15	3.07	2.87	0.54	0.58
MnO	0.03	0.04	0.02	0.02	0.02	0.02	0.01	0.01	0.03	0.04	0.03	0.02
MgO	1.16	0.50	0.85	0.03	1.04	0.35	0.29	0.09	0.81	0.28	0.22	0.02
CaO	40.83	9.13	50.74	2.47	46.62	2.67	53.15	2.41	45.03	4.50	50.79	1.77
Na_2O	0.79	0.23	1.33	0.04	0.94	0.11	1.04	0.12	0.95	0.24	0.93	0.05
K_2O	0.55	0.33	0.03	0.01	0.25	0.20	0.01	0.00	0.36	0.30	0.02	0.01
SrO	0.11	0.09	0.28	0.06	0.19	0.08	0.23	0.06	0.20	0.13	0.17	0.11
P_2O_5	26.60	6.09	28.25	1.56	27.39	2.32	25.17	2.00	27.42	2.43	26.80	2.24
SO_3	1.05	0.34	2.29	0.09	1.81	0.44	2.31	0.29	1.53	0.40	2.10	0.24
F	3.20	0.87	3.81	0.09	3.54	0.48	3.71	0.37	3.22	0.58	3.41	0.13
Cl	0.08	0.07	0.08	0.01	0.12	0.07	0.08	0.01	0.04	0.02	0.04	0.01
Cr_2O_3	0.02	0.02	0.02	0.01	0.02	0.03	0.01	0.02	0.03	0.03	0.02	0.02
BaO	0.02	0.03	0.73	0.87	0.02	0.03	0.01	0.01	0.02	0.03	0.04	0.03
Total	94.73	3.92	88.63	1.28	93.29	3.21	86.36	2.09	92.70	3.77	85.59	3.23

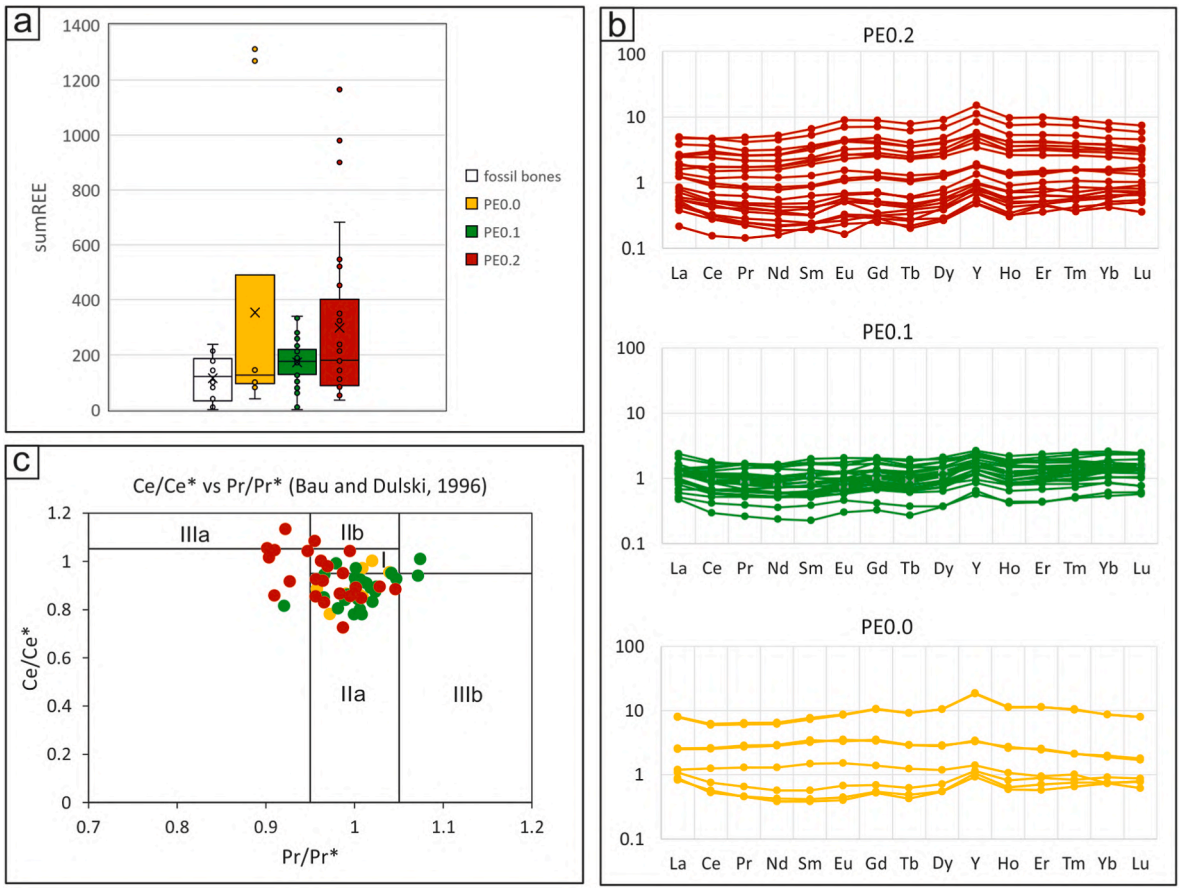

Fig. 7. REE diagrams showing the results by means of LA-ICP-MS. **a)** ΣREE box and whiskers diagram for each sample, compared to ΣREE determined in fossil bone fragments. **b)** REE patterns for phosphatic clasts of the SUB-1, YADA-2 and MH-6 samples, from PE0.0, PE0.1 and PE0.2, respectively. All data are normalized to the PAAS. **c)** $(Ce/Ce^*)_{SN}$ vs $(Pr/Pr^*)_{SN}$ diagram with fields after Bau and Dulski (1996). Note that most of the points fall in the field I (neither Ce_{SN} nor La_{SN} anomaly) and in the field IIa (positive La_{SN} anomaly, no Ce_{SN} anomaly).

abundances fall within the 675–1000 ppm range.

The in-situ trace element analysis on phosphatic minerals in phosphorite nodules and cements result in ΣREE up to 1300 ppm, with a mean value of 250 ppm (Table S2). The REE total content is higher in the phosphatic clasts than in the fossil bone fragments (Fig. 7a). The REE and Y patterns normalized to PAAS are rather similar in the different samples, scarcely fractionated and with positive Y anomaly (Fig. 7b). The Ce anomaly can be evaluated to be negligible, considering the Ce/Ce* vs Pr/Pr* diagram as suggested by Bau and Dulski (1996) (Fig. 7c).

The bone fragments display a lower LREE/HREE and a REE pattern that is closer to that of seawater compared to the phosphatic material. In the La/Yb vs. La/Sm diagram, the phosphatic material exhibits higher LREE compared to the bone materials, which in turn partially overlap with the seawater values. The enrichment in La causes part of the bone analyses to display a higher La/Sm compared to seawater (Fig. 8).

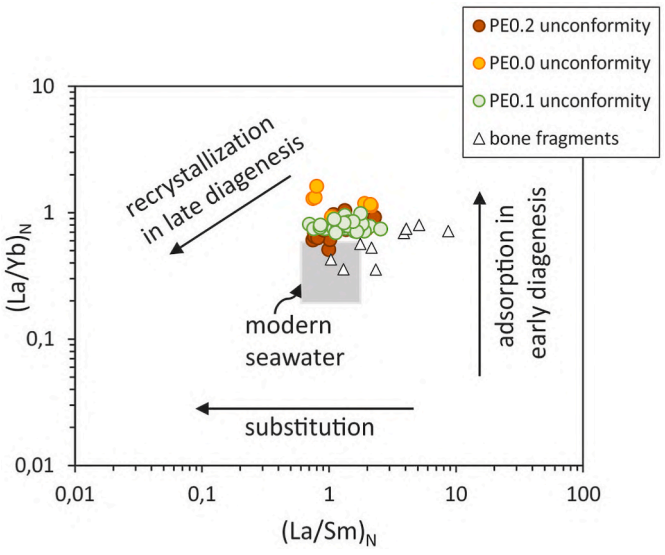

Fig. 8. $(La/Yb)_N$ vs $(La/Sm)_N$ of the analyzed phosphorites and fossil bones compared to the field of seawater. Paths produced by processes acting in early and protracted diagenesis and recrystallization are also indicated (Alibo and Nozaki, 1999; Reynard and Balter, 2014).

5. The origin of Pisco phosphorites

5.1. Phosphogenetic mechanism

The Peru-Chile margin is regarded as one of the most significant areas of marine phosphogenesis, considering both modern and ancient environments. Since the 1970s, several lines of evidence have been brought to demonstrate that phosphogenesis still occurs today in this region, including U-series dating on phosphorite nodules (Veeh et al., 1973; Baturin et al., 1976; Burnett and Veeh, 1977), the replacement of the calcium carbonate shells of benthic foraminifera by phosphates (Manheim et al., 1975), the occurrence of extant diatom species within the phosphorite nodules (Baturin et al., 1976), and $^{87}Sr/^{86}Sr$ values that match that of modern marine seawater (McArthur et al., 1990).

In the East Pisco Basin, onshore phosphorite deposits can be found in

the Ica Desert area, near Ocucaje, as first reported by Lisson (1898) and recently by Gallarday (2009), Zegarra and Canales (2013), and Castañeda and Rivera (2016). These deposits indicate that phosphogenesis has occurred in this region since the geological past. Our field observations suggests that the Ica Desert phosphorites concentrate in transgressive lags mantling each stratigraphic unconformity of the sedimentary succession throughout the Miocene and possibly earlier. In this work, we analyzed phosphorite deposits of the Miocene Pisco Formation, found on the stratigraphic unconformities PE0.0, PE0.1, and PE0.2. In these heterogeneous deposits, the dolomite and hydroxyapatite/fluorapatite occur along with calcite and other minerals typical of terrigenous components, which probably come from the sediment particles. In addition, gypsum/anhydrite and clay minerals are also found. The phosphates occur as authigenic phosphate intraclasts and small nodules, shark teeth, and marine vertebrate bone fragments. All the analyzed authigenic phosphates are composed of fluorapatite and have mean P_2O_5 and F contents of ca. 27 wt% and 3 wt%, respectively. This is concordant with the Holocene phosphorites sampled from the sea floor off the coasts of Peru and Chile by Burnett (1977) who analyzed phosphate clasts, phosphatic ovules and other allogenic components and reported that the major phosphate component is a fluorine-rich variety of apatite. The major element compositional data are in overall agreement with the chemical data that have previously been recorded from the region (Castañeda and Rivera, 2016), but our new samples seem to be relatively poor in silica, alumina and alkali with respect to most of the previous analyses, thus indicating a lower involvement of terrigenous materials. The higher CaO/P_2O_5, in turn, indicates a higher fraction of calcite and dolomite cement. Considering the lateral variability of the phosphorite layers in the Ica River valley, it is possible that the observed differences are due to local specificities of the sampling sites.

In the Pisco samples, REE patterns in phosphate intraclasts and nodules indicate an early diagenetic imprint and suboxic conditions (Figs. 7 and 8), which in turn suggest an early precipitation within the sediment. All the detected authigenic minerals formed originally at and just beneath the seafloor, close to the sediment-water interface, which is the main locus of phosphogenesis (Föllmi, 1996). In good agreement with Burnett (1977), our results support the notion that apatite precipitates out of solution rather than replacing previously existing materials: in fact, no carbonate material (e.g., foraminifera shells) has ever been found replaced by phosphate minerals in our samples. In this sense, Burnett et al. (1982) argued that nodule growth rates, together with other considerations, suggest a precipitation from the sediment interstitial waters rather than from bottom waters. To support this, Glenn and Arthur (1988) hypothesized a precipitation of CFA (carbonate--fluorapatite) from the porewaters within the upper few tens of centimeters of the sediments with a periodic sediment winnowing that maintains these structures close the sediment-water interface. In addition, Pufahl and Grimm (2003) identified the zone of active phosphate precipitation (i.e., the zone of phosphogenesis, or ZOP) with the uppermost 5–20 cm of the sediment column, thus confirming the phosphate precipitation in porewaters.

Three main mechanisms and sources contribute to the rise of the phosphorous concentration in porewater and thus lead to phosphogenesis, namely: i) the microbial degradation of buried organic matter, which liberates P; ii) the redox-driven phosphate desorption from iron and manganese oxyhydroxides settling from the oxygenated water column; and iii) the polyphosphate metabolism of large polyphosphate-accumulating sulfide-oxidizing bacteria (Föllmi, 1996; Arning et al., 2009a; Cosmidis et al., 2013). In the East Pisco Basin, the mechanisms i) and iii) are the main processes that lead to the phosphogenesis, as supported by our results as well as by previous works. In particular, Suess (1981) and Froelich et al. (1988) highlighted the role of the dissolution of fish debris at the seafloor in the Peruvian modern sediments. As initially proposed by Kazakov (1937), and later confirmed by different studies investigating the relationship between nutrient-rich water and authigenic phosphates (Ruttenberg and Berner, 1993; Slomp et al., 2002; Reynaud and James, 2012; Auer et al., 2016; Coletti et al., 2017), a strong connection can be found between phosphogenesis and upwelling, especially along the Peru-Chile continental margin (e.g., Baturin et al., 1976). As also observed by Föllmi (1996), for modern phosphorite formation in regions characterized by intense primary productivity, such as the Peruvian margin, organic matter decomposition is probably more relevant than iron and manganese redox cycles. During Miocene times, when the Pisco Formation sediments were deposited, the Peruvian margin was characterized by a complex ecosystem driven by upwelling and abundant schooling fishes that may record an early phase of the modern Humboldt Current Ecosystem (Collareta et al., 2021b), with frequent deposition of volcanic ashes that could increase nutrient availability (Gao et al., 2018; Bosio et al., 2019). A high level of primary productivity may have supported a high flux of organic matter towards the seafloor. Phosphorous can be liberated through the degradation of organic matter shortly below the sediment-water boundary, where the low oxygen conditions and high P concentration could favor the precipitation of Ca-phosphate and, with increasing alkalinity caused by sulfate reduction, primary dolomite, as testified by the observation of dolomite layers with phosphatic nodules in the Pisco Formation (Malinverno et al., 2023: Fig. 4f–h).

Focusing on the third mechanism, in one of our samples (i.e., IN-F3) phosphatic laminites were observed in the cavities of phosphate intraclasts. They can be interpreted as hardgrounds, as in the Miocene Monterey Formation that crops out along the coast of California between Los Angeles and San Francisco (Berndmeyer et al., 2012). Similarities between the Monterey and Pisco formations have already been highlighted in the past, first and foremost with respect to their marine vertebrate fossil contents, diatom-rich deposits and dolomite layers (e.g., Marty et al., 1987; Marty, 1989; Dunbar et al., 1990; Malinverno et al., 2023). Regarding the laminites within the inner phosphate cavities, the latter offer calm and relatively undisturbed settings, even under quite dynamic conditions. This environment facilitated the uninterrupted growth of phosphatic laminite over prolonged periods, interrupted only by occasional sediment influx that affected the growth of laminites by diluting the P concentration (Berndmeyer et al., 2012). The occurrence of laminites in Peruvian phosphate sediments has been reported also by Arning et al. (2009a, b) and interpreted as the evidence of bacterial activity involved in the phosphogenetic process (as formerly speculated by Froelich et al., 1988). Arning et al. (2009a, b) suggested that the autochthonous phosphatic laminites are the result of the activity of both sulfate-reducing bacteria and sulfide-oxidizing bacteria such as *Thioploca*, *Beggiatoa* and *Thiomargarita* (e.g., Gallardo, 1977; Ferdelman et al., 1997; Jørgensen and Gallardo, 1999; Suits and Arthur, 2000; Zopfi et al., 2008; Bailey et al., 2013; Dela Pierre et al., 2015; Smrzka et al. 2024), and the same could be hypothesize with respect to our samples. The combined activity of closely associated sulfide-oxidizing bacteria, known to be capable of liberating phosphate, and sulfate-reducing bacteria have the potential to drive phosphogenesis in marine sediments below high productivity zones (Arning et al., 2007, 2009a). The degradation of organic matter by sulfate-reducing bacteria has the potential to liberate in the porewaters the phosphorus needed for phosphogenesis (Soudry and Lewy, 1988; Schulz and Schulz, 2005; Al-Bassam and Halodová, 2018). This process may have acted in phosphogenic settings over the last 600 million years at least (Bailey et al., 2013; Smrzka et al., 2024). If the presence sulfide-oxidizing bacteria such as *Thioploca* (which occurs abundantly in the modern Peruvian shelf) has only been hypothesized with respect to the Miocene Pisco embayment (Bosio et al., 2021b), and now testified by the presence of laminites in Miocene phosphorite deposits, that of sulfate-reducing bacteria is widely attested in the Miocene record of the East Pisco Basin (Gariboldi et al., 2015; Bosio et al., 2021a, 2021b; Malinverno et al., 2023). In our samples, sulfate-reducing bacterial activity is supported by the presence of framboidal Fe-oxyhydroxides interpreted as “pyrite ghosts”, also reported by Glenn and Arthur (1988) and Cosmidis et al. (2013), who suggest pyrite biomorphs to be an evidence of a

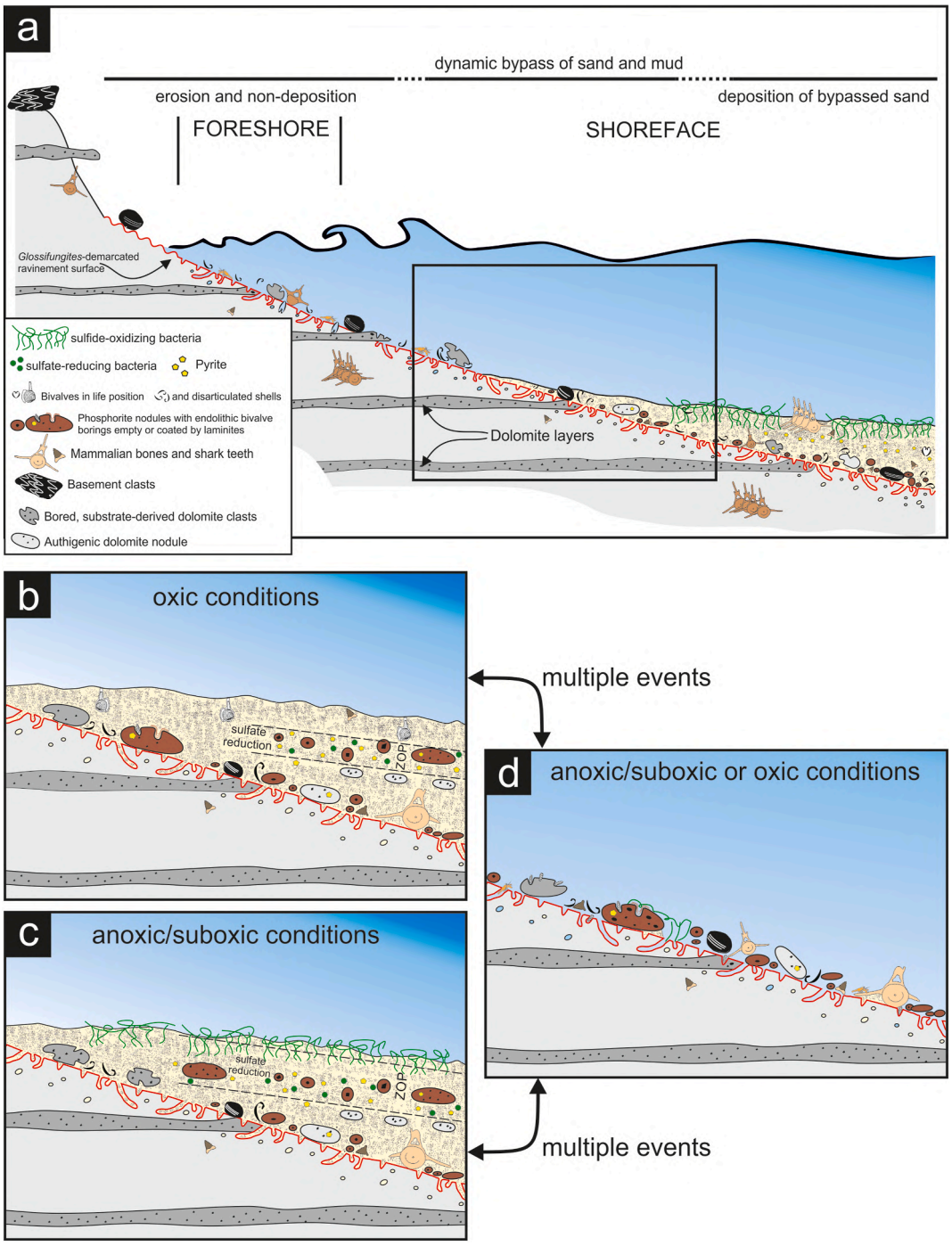

Fig. 9. Schematic representation of the transgressive sedimentary regime during phosphorite accumulation by dynamic bypassing. In the Pisco Formation, the phosphorite-rich concentrations lie along distinctive discontinuity surfaces identified as transgressive ravinement surfaces by independent physical stratigraphic evidence. a) Idealized nearshore profile during transgression characterized by the co-existence of: i) an onshore, presumably foreshore to upper shoreface environment of erosional ravinement (Zecchin et al., 2019), recording a period of erosion and omission evidenced by a *Glossifungites* Ichnofacies (firmground). In this setting, skeletal material, dolomite and basement pebbles and cobbles were exhumed from the underlying strata and reworked; ii) a lower shoreface area characterized by regimes of low net rates of siliciclastic accumulation resulting from alternating deposition of sediment increments and erosional winnowing of the seafloor (i.e., dynamic sediment bypass), generating the multiple-event, base-of-cycle phosphorite-rich concentration; iii) a deeper area serving as a sink for bypassed sediment where net depositional rates are positive and sedimentary dynamic is not able to produce phosphate-rich hiatal concentrations. b, c), In the central portion of the nearshore profile (black square in "a"), relatively thin (decimeter-scale) depositional increments develop a zone of active phosphate precipitation (ZOP) at very shallow burial levels in either oxic or anoxic/suboxic conditions at the seafloor. d) In this setting, however, depositional increments fail to accumulate permanently and are balanced or nearly balanced by episodes of erosion that winnowed, reworked and telescoped short-term phosphorite concentrations into a major basal layer. Evidence of bioerosion on phosphatic grains aligns with the notion that, following concentration, they resided at the seafloor for some time before reburial.

microbial activity in the phosphorite crusts of the Peruvian shelf. The precipitation of apatite rather than calcium carbonates tends to be favored in reducing, neutral or slightly acidic waters (Coleman, 1985; Berndmeyer et al., 2012). The REE patterns and redox-sensitive element composition in the Pisco samples confirm the precipitation of phosphorites under suboxic conditions in the porewaters showing a negligible Ce anomaly, while displaying an early diagenetic imprint that enriched the phosphate in REE (Figs. 7 and 8) following Bau and Dulski (1996) and Haley et al. (2004).

Four main types of authigenic phosphorite grains can be identified in the deposits analyzed in this work, namely: i) relatively common phosphate nodules with a single nucleus surrounded by fluorapatite, similar to the redox-aggregated grains (RA grains) described by Pufahl and Grimm (2003); ii) abundant phosphate intraclasts, with terrigenous particles and rare microfossils cemented by fluorapatite; iii) rare phosphate intraclasts formed by small fluorapatite nodules and coated by phosphatic laminite; iv) rare phosphate intraclasts with burrows coated by phosphatic laminites, similar to those described by Arning et al. (2009a) and by Berndmeyer et al. (2012). As for the first such type, i.e. fluorapatite nodules with a single nucleus, Pufahl and Grimm (2003) hypothesized that RA grains may have been produced by apatite precipitation within the ZOP as a consequence of changes in porewater redox conditions. This process does not necessitate exhumation and reburial of grains into the ZOP, but instead only requires a variable flux of organic carbon to the seafloor (Fig. 9). On the contrary, for the other phosphorite grain types (i.e. the phosphate intraclasts), multiple episodes of phosphatization, exhumation, and erosion should be hypothesized (Pufahl and Grimm, 2003) (see Chapter below). Moreover, the grains of the third and fourth type (i.e., those formed by small phosphate nodules or presenting burrows with laminite) evoke multiple phases of phosphogenesis and reworking on the seafloor (see Fig. 9).

Besides the phosphate grains, dolomite-cemented intraclasts – which often display borings –dolomite internal molds of gastropods and articulated bivalves are also found in the Pisco phosphorite deposits. In the East Pisco Basin, and especially in the Pisco Formation, dolomite is commonly found in different settings: surrounding fossil vertebrate remains and filling their internal cavities (Gariboldi et al., 2015); forming internal, external and compound molds of invertebrate shells (Bosio et al., 2021a); and forming laterally-continuous horizons that at least in one case cemented small phosphate nodules (Malinverno et al., 2023). Dolomite precipitation is linked to early diagenesis at low temperatures, being commonly observed in upwelling settings, where high primary productivity leads to substantial organic carbon flux to the seafloor, thus contributing to cyclical oxygen depletion at the bottom (Baker and Burns, 1985; Petrash et al., 2017). Dolomite formed in the bacterial sulfate reduction and methanogenesis zones at depths just below those at which phosphogenesis occurred (Glenn and Arthur, 1988), where the increase of alkalinity (due to high concentrations of HCO_3^-) may prevent further precipitation of fluorapatite while favoring dolomite formation. High concentrations of dissolved sulfate in seawater inhibit dolomite formation (Baker and Kastner, 1981), while microbially-mediated sulfate reduction effectively decreases the inhibitory effect of sulfate ions while simultaneously leading to an increase in alkalinity and primary dolomite precipitation (e.g., Compton, 1988). Thus, microbial activity at the seafloor plays a major role in controlling both phosphate and dolomite precipitation during the early diagenesis, hence the formation of Ca-phosphate and dolomite nodules in close spatial relationship yet in distinct geochemical environments.

5.2. Sedimentary regime

The heterogeneous composition of the Pisco phosphorite-rich deposits and the nature of the erosional surfaces on which they lay suggest multiple phases of phosphogenesis and erosional events in a shallow-marine depositional setting characterized by low net rates of sediment accumulation. Garrison and Kastner (1990) associated carbonate fluorapatite precipitation on the shelf and upper slope off Peru with early diagenesis, erosion, exhumation, reburial and re-phosphatization processes, associated with changing energy conditions.

According to Pufahl and Grimm (2003), phosphate grains formation requires a long residence time just below the sediment-water interface: if the sedimentation rate is excessively high, grains undergo rapid burial and are consequently displaced from the ZOP. Therefore, long residence times near the sediment-water interface as well as periods of stratigraphic condensation are necessary. Low sedimentation rates and repeated reworking of the seafloor facilitate phosphogenesis by allowing for the buildup of porewater phosphate (Föllmi et al., 1991). According to Glenn and Arthur (1988) and Glenn et al. (1994), periodic sediment reorganization (e.g., via bioturbation, current winnowing of fine-grained sediment, and mass wasting) plays an important role both in concentrating phosphate grains and in maintaining nodules and crusts at critical depth levels in the sediment. An important reworking in the form of gravity flows is hypothesized by Föllmi et al. (2008) for the Oligocene to Miocene phosphate rich-sediments in Malta and south-eastern Sicily.

In our study, the intimate association of phosphate- and dolomite-cemented intraclasts, shark teeth, polished bone fragments, pebble-to boulder-size basement clasts, mollusk shell molds and clasts exhibiting bivalve borings is suggestive of concentration of phosphate clasts during periods of low net sedimentation. For this reason, the Pisco phosphorite deposits would fall within the “condensed phosphates” class of Föllmi (1996, 2016), in which multiple stages of phosphogenesis are interrupted by episodes of winnowing and reworking (Saltzman, 2003). The presence of intraclasts suggests substrate reworking or winnowing by storms, episodic undercurrents, or shallow-water currents (Garrison and Kastner, 1990; Garzanti, 1993; Pufahl and Grimm, 2003; Pufahl et al., 2003). However, the texture of the Pisco phosphorite layers indicates condensation under a regime of dynamic bypassing rather than complete sediment starvation (Kidwell, 1989), where repeated cycles of deposition of sediment increments and winnowing of finer grains concentrated different generations of phosphatic clasts and other components (Fig. 9). Following Kidwell (1989), during condensation by dynamic bypassing clasts and shells are not necessarily exposed to destructive agents continuously. Exposure may be only brief and episodic, alternating with relatively prolonged periods of burial below the surficial zone of traction and active bioturbation (Kidwell, 1989).

Discrete phosphorite beds can form at shallow burial levels during early transgression phases (Marshall-Neill and Ruffell, 2004; Rismyhr et al., 2018) at times when the porewaters are enriched in phosphate due to the presence of organic-rich sediments, as typical of upwelling settings (Salama et al., 2015). In particular, the recognition of a *Glossifungites* Ichnofacies dominated by *Thalassinoides*, *Gyrolithes* and *Gastrochaenolites* filled by phosphorite elements records unconformities associated with abrupt seaward shifts in facies (Pemberton et al., 2004; MacEachern et al., 1992). These unconformities are interpreted as polygenetic surfaces that formed by subaerial erosion during sea-level lowstands and were subsequently modified during erosional transgression (Di Celma et al., 2022) (Fig. 9).

In the Pisco Formation, phosphorite-rich concentrations are found along distinctive discontinuity surfaces, which have been identified as transgressive ravinement surfaces based on independent physical stratigraphic evidence. In Fig. 9a, an idealized Pisco nearshore profile is drawn. During transgression, this nearshore setting is characterized by the co-existence of three environmental scenarios: i) an onshore, presumably foreshore to upper shoreface domain of erosional ravinement (Zecchin et al., 2019); ii) a lower shoreface area characterized by regimes of low net rates of siliciclastic accumulation; and iii) a deeper domain serving as a sink for bypassed sediment. The first such environment documents a period of erosion and omission indicated by the presence of a *Glossifungites* Ichnofacies, which in turn suggests the development of a firmground. Here, skeletal material, dolomite concretions, and basement pebbles and cobbles are unearthed from the

underlying strata and reworked. The lower shoreface zone is characterized by alternating deposition of sediment increments and erosional winnowing of the seafloor, known as dynamic sediment bypass (Kidwell, 1989), which leads to the accumulation of phosphorite-rich concentrations at the base of each cycle. In the deeper area, positive net depositional rates prevail, and the sedimentary dynamics do not yield phosphate-rich hiatus concentrations. Fig. 9b and 9c provide a focus on the central portion of the nearshore profile (black square in Fig. 9a). Within this zone, thin depositional increments, typically on a decimeter scale, give rise to a zone of active phosphate precipitation (ZOP) at extremely shallow burial depths. Nevertheless, in this context, depositional increments do not accumulate permanently. Instead, they are offset or nearly offset by episodes of erosion that winnow, rework, and telescope short-term phosphorite concentrations into a major basal layer (Fig. 9d). In summary, multiple phases of extensive Ca-phosphate precipitation alternated with erosional phases of winnowing at the base of the Pisco Formation depositional sequences during early transgressions. These repeated cycles of deposition and erosion allowed for increasing the concentration of intraclasts and other components in concurrence with primary phosphogenetic grains at the ravinement surface during the very early phase of transgression (Fig. 9). As the transgression proceeded and the water-depth increased, the net sedimentation rate became too high for dynamic bypassing to be effective and the ravinement surface and the overlying phosphate-rich hiatal interval were definitively buried. Phosphate and dolomite precipitation continued within the directly overlying sediment, but in the absence of an efficient concentration mechanism, its products were probably "diluted" into the accumulating sediment, as testified by the sparse yet frequent occurrence of dolomite and subordinately phosphorite nodules within the sediment (Malinverno et al., 2023).

Finally, post-depositional cementation then occurred. Our results suggest that all the components of the Pisco phosphorite deposits were finally cemented by dolomite, calcite, silica, gypsum/anhydrite and baryte cements that precipitated during subsequent stages of early and late diagenesis.

6. Conclusions

This work sheds light on the genesis of Miocene phosphorite layers in the East Pisco Basin. Typically, phosphorites lie on a sharp and irregular erosional surface interpreted as a wave-ravinement surface demarcated by a substrate-controlled *Glossifungites* Ichnofacies at the base of distinct depositional sequences. They appear as a variable mixture of pebble-to boulder-size basement crystalline clasts, granule-to pebble-size phosphatic clasts and nodules, cobble-sized dolomite clasts featuring bivalve borings, shark teeth, internal molds of gastropods and articulated bivalves, polished marine vertebrate bone fragments, and partially articulated skeletons of marine mammals. The phosphatic clasts and nodules are made of detrital crystals or fossil fragments encased in fluorapatite. Dolomite-cemented clasts are also present, which are usually coated by Fe-oxyhydroxides. The mineralogical, geochemical and textural relationships point to deposition in a shallow-marine environment marked by elevated biological productivity and low sedimentation rates, with phosphogenesis occurring just below the water-sediment interface in suboxic conditions, in close relationship with microbial activity and primary dolomite precipitation. Owing to their heterogeneous nature and their occurrence in association with erosional surfaces, the Pisco phosphorite deposits are inferred to have accumulated under multiple phases of phosphogenesis and erosional events of the seafloor due to the action of waves and storm-related flows, low net deposition due to sediment bypass during shoreface retreat and physico-chemical conditions favoring their development. This study not only enhances our understanding of the genesis of phosphorite layer in the East Pisco Basin, but also underscores the intricate interplay among the processes beneath. Hopefully, such insights will contribute to deciphering the geological significance of these sedimentary rocks and informing for potential economic applications.

Funding

This study was funded by the Postdoctoral Research Grant Scheme 2022 of the IAS (International Association of Sedimentologists) to G.Bo. We acknowledge financial support under the National Recovery and Resilience Plan (NRRP), Mission 4, Component 2, Investment 1.1, Call for tender No. 104 published on February 02, 2022 by the Italian Ministry of University and Research (MUR), funded by the European Union – NextGenerationEU – Project Title: BIOVERTICES (BIOdiversity of VERTebrates In the CEnozoic Sea) – CUP I53D23002070 006 - Grant Assignment Decree No. 965 adopted on June 30, 2023 by the Italian Ministry of University and Research (MUR).

CRediT authorship contribution statement

Giulia Bosio: Writing – review & editing, Writing – original draft, Visualization, Validation, Resources, Project administration, Methodology, Investigation, Funding acquisition, Formal analysis, Data curation, Conceptualization. **Anna Gioncada:** Writing – review & editing, Writing – original draft, Visualization, Validation, Supervision, Resources, Project administration, Methodology, Investigation, Formal analysis, Data curation, Conceptualization. **Elisa Malinverno:** Writing – review & editing, Validation, Supervision, Resources, Investigation, Formal analysis, Data curation, Conceptualization. **Giovanni Coletti:** Writing – review & editing, Visualization, Validation, Resources, Investigation, Formal analysis. **Alberto Collareta:** Writing – review & editing, Visualization, Validation, Resources, Investigation, Funding acquisition, Formal analysis. **Luca Mariani:** Writing – review & editing, Visualization, Validation, Investigation, Formal analysis. **Alessandro Cavallo:** Writing – review & editing, Validation, Methodology, Investigation, Formal analysis. **Giovanni Bianucci:** Writing – review & editing, Visualization, Validation, Resources, Investigation. **Mario Urbina:** Writing – review & editing, Visualization, Validation, Resources. **Claudio Di Celma:** Writing – review & editing, Writing – original draft, Visualization, Validation, Supervision, Resources, Project administration, Investigation, Formal analysis, Data curation, Conceptualization.

Declaration of competing interest

The authors declare that they have no known competing financial interests or personal relationships that could have appeared to influence the work reported in this paper.

Data availability

All the data are reported in the main text of the paper and in the Supplementary Material.

Acknowledgments

The authors would like to thank Carlo Alberto Brunetti for his help in preparing and describing phosphorite samples, Andrea Risplendente for the EPMA analyses, and Gianluca Sessa for the LA-ICP-MS analyses. The authors wish to thank TS Lab & Geoservices snc for realizing thin sections. A special thanks also to Rafael Varas-Malca for his help during fieldwork. We would also thank the Editor Istvan Csato and two anonymous reviewers for improving the final version of the manuscript.

Appendix A. Supplementary data

Supplementary data to this article can be found online at https://doi.org/10.1016/j.marpetgeo.2024.106941.

References

Auer, G., Hauzenberger, C.A., Reuter, M., Piller, W.E., 2016. Orbitally paced phosphogenesis in M editerranean shallow marine carbonates during the middle Miocene Monterey event. G-cubed 17, 1492–1510.

Al-Bassam, K., Halodová, P., 2018. Fossil bacteria in cenomanian–turonian phosphate nodules and coprolites, bohemian bretaceous basin, Czech republic. Ann. Soc. Geol. Pol. 88, 257–272.

Alibo, D.S., Nozaki, Y., 1999. Rare earth elements in seawater: particle association, shale normalization, and Ce oxidation. Geochem. Cosmochim. Acta 63, 363–372. https://doi.org/10.1016/S0016-7037(98)00279-8.

Arning, E.T., Birgel, D., Schulz-Vogt, H.N., Jørgensen, B.B., Peckmann, J., 2007. Phosphogenesis in recent upwelling areas: the importance of microbial communities indicated by lipid biomarkers. Geochem. Cosmochim. Acta 71 (15 Suppl. Suppl. S), A37. A37.

Arning, E.T., Birgel, D., Brunner, B., Peckmann, J., 2009a. Bacterial formation of phosphatic laminites off Peru. Geobiology 7, 295–307.

Arning, E.T., Lückge, A., Breuer, L.C., Gussone, N., Birgel, D., Peckmann, J., 2009b. Genesis of phosphorite crusts off Peru. Mar. Geol. 262, 68–81.

Baker, K.B., Burnett, W.C., 1988. Distribution, texture and composition of modern phosphate pellets in Peru shelf muds. Mar. Geol. 80, 195–213.

Baker, P.A., Burns, S.J., 1985. Occurrence and formation of dolomite in organic-rich continental margin sediments. AAPG (Am. Assoc. Pet. Geol.) Bull. 69, 1917–1930.

Bailey, J.V., Corsetti, F.A., Greene, S.E., Crosby, C.H., Liu, P., Orphan, V.J., 2013. Filamentous sulfur bacteria preserved in modern and ancient phosphatic sediments: implications for the role of oxygen and bacteria in phosphogenesis. Geobiology 11, 397–405.

Baturin, G.N., Bliskovskiy, V.Z., Lisitsyn, A.P., 1976. Upper Quaternary phosphorite nodules off the coast of Peru. Oceanology 15, 331–333.

Baturin, G.N., Bezrukov, P.L., 1979. Phosphorites on the sea floor and their origin. Mar. Geol. 31, 317–332.

Baker, P.A., Kastner, M., 1981. Constraints on the formation of sedimentary dolomite. Science 213 (4504), 214–216.

Baturin, G.N., 1982. Phosphorites on the Sea Floor. Elsevier.

Bau, M., Dulski, P., 1996. Distribution of yttrium and rare-earth elements in the penge and kuruman iron-formations, transvaal supergroup, South Africa. Precambrian Res. 79, 37–55.

Bech, J., Suarez, M., Reverter, F., Tume, P., Sánchez, P., Bech, J., Lansac, A., 2010. Selenium and other trace elements in phosphate rock of Bayovar–Sechura (Peru). J. Geochem. Explor. 107, 136–145.

Berndmeyer, C., Birgel, D., Brunner, B., Wehrmann, L.M., Jöns, N., Bach, W., Arning, E. T., Föllmi, K.B., Peckmann, J., 2012. The influence of bacterial activity on phosphorite formation in the Miocene Monterey Formation, California. Palaeogeogr. Palaeoclimatol. Palaeoecol. 317, 171–181.

Bianucci, G., Bosio, G., Malinverno, E., De Muizon, C., Villa, I.M., Urbina, M., Lambert, O., 2018. A new large squalodelphinid (Cetacea, Odontoceti) from Peru sheds light on the Early Miocene platanistoid disparity and ecology. R. Soc. Open Sci. 5, 172302.

Bianucci, G., Collareta, A., 2022. An overview of the fossil record of cetaceans from the East Pisco Basin (Peru). Boll. Soc. PaleontoI. Ital 61, 20.

Bosio, G., Bianucci, G., Collareta, A., Landini, W., Urbina, M., Di Celma, C., 2022. Ultrastructure, composition, and $^{87}Sr/^{86}Sr$ dating of shark teeth from lower Miocene sediments of southern Peru. J. S. Am. Earth Sci. 118, 103909.

Bosio, G., Gioncada, A., Malinverno, E., Di Celma, C., Villa, I.M., Cataldi, G., Gariboldi, K., Collareta, A., Urbina, M., Bianucci, G., 2019. Chemical and petrographic fingerprinting of volcanic ashes as a tool for high-resolution stratigraphy of the upper Miocene Pisco Formation (Peru). J. Geol. Soc. 176, 13–28. https://doi.org/10.1144/jgs2018-071. London.

Bosio, G., Malinverno, E., Collareta, A., Di Celma, C., Gioncada, A., Parente, M., Berra, F., Marx, F.G., Vertino, A., Urbina, M., Bianucci, G., 2020b. Strontium isotope stratigraphy and the thermophilic fossil fauna from the middle miocene of the East Pisco basin (Peru). J. S. Am. Earth Sci. 97, 102399 https://doi.org/10.1016/j.jsames.2019.102399.

Bosio, G., Malinverno, E., Villa, I.M., Di Celma, C., Gariboldi, K., Gioncada, A., Barberini, V., Urbina, M., Bianucci, G., 2020c. Tephrochronology and chronostratigraphy of the miocene Chilcatay and Pisco formations (East Pisco basin, Peru). Newsl. Stratigr. 53, 213–247. https://doi.org/10.1127/nos/2019/0525.

Bosio, G., Bracchi, V., Malinverno, E., Collareta, A., Coletti, G., Gioncada, A., Kočí, T., Di Celma, C., Bianucci, G., Basso, D., 2021a. Taphonomy of a *Panopea* Ménard de la Groye, 1807 shell bed from the Pisco Formation (Miocene, Peru)[Taphonomie d'une couche de coquilles de *Panopea* Ménard de la Groye, 1807 de la Formation Pisco (Miocène, Pérou).]. Comptes Rendus Palevol 20 (8), 119–140.

Bosio, G., Collareta, A., Di Celma, C., Lambert, O., Marx, F.G., de Muizon, C., Gioncada, A., Malinverno, E., Varas Malca, R., Urbina, M., Bianucci, G., 2021b. Taphonomy of marine vertebrates of the Pisco Formation (miocene, Peru): insights into the origin of an outstanding fossil-lagerstätte. PLoS One 16 (7), e0254395.

Bosio, G., Gioncada, A., Gariboldi, K., Bonaccorsi, E., Collareta, A., Pasero, M., Di Celma, C., Malinverno, E., Urbina, M., Bianucci, G., 2021c. Mineralogical and geochemical characterization of fossil bones from a Miocene marine Konservat-Lagerstätte. J. S. Am. Earth Sci. 105, 102924 https://doi.org/10.1016/j.jsames.2020.102924.

Bruggmann, S., Gilleaudeau, G.J., Romaniello, S.J., Severmann, S., Canfield, D.E., Anbar, A.D., Scholz, F., Frei, R., 2022. Uranium isotope cycling on the highly productive Peruvian margin. Chem. Geol. 590, 120705.

Burnett, W.C., 1977. Geochemistry and origin of phosphorite deposits from off Peru and Chile. Geol. Soc. Am. Bull. 88, 813–823.

Burnett, W.C., 1980. Apatite-glauconite associations off Peru and Chile: palaeooceanographic implications. J. Geol. Soc. 137, 757–764.

Burnett, W.C., Riggs, S.R., 1990. Phosphate Deposits of the World, Volume 3, Neogene to Modern Phosphorites. Cambridge University Press, Cambridge, p. 464.

Burnett, W.C., Veeh, H.H., 1977. Uranium-series disequilibrium studies in phosphorite nodules from the west coast of South America. Geochem. Cosmochim. Acta 41, 755–764.

Burnett, W.C., Beers, M.J., Roe, K.K., 1982. Growth rates of phosphate nodules from the continental margin off Peru. Science 215, 1616–1618.

Burnett, W.C., Roe, K.K., Piper, D.Z., 1983. Upwelling and phosphorite formation in the ocean. In: Suess, E., Thiede, J. (Eds.), Coastal Upwelling its Sediment Record - Part A: Responses of the Sedimentary Regime to Present Coastal Upwelling. Plenum Press, New York, pp. 377–397.

Castañeda, F.A., Rivera, L.R., 2016. Las fosforitas del Mioceno y su relación con el contenido económico de los fosfatos de Pisco y Sechura (Perú). Revista del Instituto de Investigación de la Facultad de Ingeniería Geológica, Minera. Metalúrgica y Geográfica 19 (37).

Cheney, T.M., McClellan, G.H., Montgomery, E.S., 1979. Sechura phosphate deposits, their stratigraphy, origin, and composition. Econ. Geol. 74, 232–259.

Clift, P.D., Hartley, A.J., 2007. Slow rates of subduction erosion and coastal underplating along the Andean margin of Chile and Peru. Geology 35, 503–506. https://doi.org/10.1130/G23584A.1.

Clift, P.D., Vannucchi, P., 2004. Controls on tectonic accretion versus erosion in subduction zones: implications for the origin and recycling of the continental crust. Rev. Geophys. 42, 2003RG000127.

Coleman, M.L., 1985. Geochemistry of diagenetic non-silicate minerals: kinetic considerations. Phil. Trans. Roy. Soc. Lond. Math. Phys. Sci. 315, 39–56.

Coletti, G., El Kateb, A., Basso, D., Cavallo, A., Spezzaferri, S., 2017. Nutrient Influence on Fossil Carbonate Factories: Evidence from SEDEX Extractions on Burdigalian Limestones (Miocene, NW Italy and S France). Palæogeography, Palæoclimatology, Palæoecology, vol. 475, pp. 80–92.

Coletti, G., Bosio, G., Collareta, A., Malinverno, E., Bracchi, V., Di Celma, C., Basso, D., Stainbank, S., Spezzaferri, S., Cannings, T., Bianucci, G., 2019. Biostratigraphic, evolutionary, and paleoenvironmental significance of the southernmost lepidocyclinids of the Pacific coast of South America (East Pisco Basin, southern Peru). J. S. Am. Earth Sci. 96, 102372 https://doi.org/10.1016/j.jsames.2019.102372.

Collareta, A., Di, Celma C., Bosio, G., Pierantoni, P.P., Malinverno, E., Lambert, O., Marx, F.G., Landini, W., Urbina, M., Bianucci, G., 2021a. Distribution and paleoenvironmental framework of middle Miocene marine vertebrates along the western side of the lower Ica Valley (East Pisco Basin, Peru). J. Maps 17, 7–17. https://doi.org/10.1080/17445647.2020.1850535.

Collareta, A., Lambert, O., Marx, F.G., de Muizon, C., Varas-Malca, R., Landini, W., Bosio, G., Malinverno, E., Gariboldi, K., Gioncada, A., Urbina, M., Bianucci, G., 2021b. Vertebrate Palaeoecology of the Pisco Formation (miocene, Peru): glimpses into the ancient humboldt Current ecosystem. J. Mar. Sci. Eng. 9, 1188.

Compton, J.S., 1988. Degree of supersaturation and precipitation of organogenic dolomite. Geology 16, 318–321.

Cook, P.J., Shergold, J.H., 1986. Phosphate Deposits of the World, Proterozoic and Cambrian Phosphorites. Cambridge University Press, Cambridge, p. 386.

Cordell, D., Drangert, J.O., White, S., 2009. The story of phosphorus: global food security and food for thought. Global Environ. Change 19, 292–305.

Cosmidis, J., Benzerara, K., Menguy, N., Arning, E., 2013. Microscopy evidence of bacterial microfossils in phosphorite crusts of the Peruvian shelf: implications for phosphogenesis mechanisms. Chem. Geol. 359, 10–22.

Cullen, D.J., Burnett, W.C., 1986. Phosphorite associations on seamounts in the tropical southwest Pacific Ocean. Mar. Geol. 71, 215–236.

Dela Pierre, F., Natalicchio, M., Ferrando, S., Giustetto, R., Birgel, D., Carnevale, G., Gier, S., Lozar, F., Marabello, D., Peckmann, J., 2015. Are the large filamentous microfossils preserved in Messinian gypsum colorless sulfide-oxidizing bacteria? Geology 43 (10), 855–858.

DeVries, T.J., Barron, J.A., Urbina-Schmitt, M., Ochoa, D., Esperante, R., Snee, L.W., 2021. The miocene stratigraphy of the laberinto area (río Ica valley) and its bearing on the geological history of the East Pisco basin (south-central Peru). J. S. Am. Earth Sci. 103458 https://doi.org/10.1016/j.jsames.2021.103458.

Di Celma, C., Malinverno, E., Bosio, G., Collareta, A., Gariboldi, K., Gioncada, A., Molli, G., Basso, D., Varas-Malca, R., Pierantoni, P.P., Villa, I.M., Lambert, O., Landini, W., Sarti, G., Cantalamessa, G., Urbina, M., Bianucci, G., 2017. Sequence stratigraphy and paleontology of the upper miocene Pisco Formation along the western side of the lower Ica valley (Ica Desert, Peru). Riv. Ital. Paleontol. Stratigr. 123, 255–273. https://doi.org/10.13130/2039-4942/8373.

Di Celma, C., Malinverno, E., Bosio, G., Gariboldi, K., Collareta, A., Gioncada, A., Landini, W., Pierantoni, P.P., Bianucci, G., 2018a. Intraformational unconformities as a record of late Miocene eustatic falls of sea level in the Pisco Formation (southern Peru). J. Maps 14, 607–619. https://doi.org/10.1080/17445647.2018.1517701.

Di Celma, C., Malinverno, E., Cantalamessa, G., Gioncada, A., Bosio, G., Villa, I.M., Gariboldi, K., Rustichelli, A., Pierantoni, P.P., Landini, W., Tinelli, C., Collareta, A., Bianucci, G., 2016a. Stratigraphic framework of the late miocene Pisco Formation at Cerro los Quesos (Ica Desert, Peru). J. Maps 12, 1020–1028. https://doi.org/10.1080/17445647.2015.1115783.

Di Celma, C., Malinverno, E., Gariboldi, K., Gioncada, A., Rustichelli, A., Pierantoni, P.P., Landini, W., Bosio, G., Tinelli, C., Bianucci, G., 2016b. Stratigraphic framework of the late miocene to Pliocene Pisco Formation at Cerro Colorado (Ica Desert, Peru). J. Maps 12, 515–529.

Di Celma, C., Malinverno, E., Collareta, A., Bosio, G., Gariboldi, K., Lambert, O., Landini, W., Pierantoni, P.P., Gioncada, A., Villa, I.M., Coletti, G., Muizon, C. de,

Urbina, M., Bianucci, G., 2018b. Facies analysis, stratigraphy and marine vertebrate assemblage of the lower miocene Chilcatay Formation at Ullujaya (Pisco Basin, Peru). J. Maps 14, 257–268. https://doi.org/10.1080/17445647.2018.1456490.

Di Celma, C., Pierantoni, P.P., Malinverno, E., Collareta, A., Lambert, O., Landini, W., Bosio, G., Gariboldi, K., Gioncada, A., de Muizon, C., Molli, G., Marx, F.G., Varas-Malca, R.M., Urbina, M., Bianucci, G., 2019. Allostratigraphy and paleontology of the lower miocene Chilcatay Formation in the zamaca area, East Pisco basin, southern Peru. J. Maps 15, 393–405. https://doi.org/10.1080/17445647.2019.1604439.

Di Celma, C., Pierantoni, P.P., Volatili, T., Molli, G., Mazzoli, S., Sarti, G., Ciattoni, S., Bosio, G., Malinverno, E., Collareta, A., Gariboldi, K., Gioncada, A., Jablonská, D., Landini, W., Urbina, M., Bianucci, G., 2022. Towards deciphering the cenozoic evolution of the East Pisco basin (southern Peru). J. Maps 18, 397–412.

Dunbar, R.B., Marty, R.C., Baker, P.A., 1990. Cenozoic marine sedimentation in the Sechura and Pisco basins, Peru. Palaeogeogr. Palaeoclimatol. Palaeoecol. 77 (3–4), 235–261.

Emsbo, P., McLaughlin, P.I., Breit, G.N., du Bray, E.A., Koenig, A.E., 2015. Rare earth elements in sedimentary phosphate deposits: solution to the global REE crisis? Gondwana Res. 27, 776–785.

Esperante, R., Brand, L.R., Chadwick, A.V., Poma, O., 2015. Taphonomy and paleoenvironmental conditions of deposition of fossil whales in the diatomaceous sediments of the Miocene/Pliocene Pisco Formation, southern Peru—a new fossil-lagerstätte. Palaeogeogr. Palaeoclimatol. Palaeoecol. 417, 337–370.

Ferdelman, T.G., Lee, C., Pantoja, S., Harder, J., Bebout, B.M., Fossing, H., 1997. Sulfate reduction and methanogenesis in a *Thioploca*-dominated sediment off the coast of Chile. Geochim Cosmochim Ac 61, 3065–3079, 1997.

Filippelli, G.M., 2011. Phosphate rock formation and marine phosphorus geochemistry: the deep time perspective. Chemosphere 84, 759–766.

Föllmi, K.B., 1996. The phosphorus cycle, phosphogenesis and marine phosphate-rich deposits. Earth Sci. Rev. 40, 55–124.

Föllmi, K.B., 2016. Sedimentary condensation. Earth Sci. Rev. 152, 143–180.

Föllmi, K.B., Garrison, R.E., Grimm, K.A., 1991. Stratification in phosphatic sediments: illustrations from the Neogene of California. In: Einsele, G., Ricken, W., Seilacher, A. (Eds.), Cycles and Events in Stratigraphy. Springer-Verlag, Berlin, Heidelberg, pp. 492–507.

Föllmi, K.B., Gertsch, B., Renevey, J.P., De Kaenel, E., Stille, P., 2008. Stratigraphy and sedimentology of phosphate-rich sediments in Malta and south-eastern Sicily (latest Oligocene to early Late Miocene). Sedimentology 55, 1029–1051.

Frohlich, P.N., Kim, K.H., Jahnke, R., Burnett, W.C., Soutar, A., Deakin, M., 1983. Pore water fluoride in Peru continental margin sediments: uptake from seawater. Geochem. Cosmochim. Acta 47, 1605–1612.

Froelich, P.N., Arthur, M.A., Burnett, W.C., Deakin, M., Hensley, V., Jahnke, R., Kaul, L., Kim, K.H., Roe, K., Soutar, A., Vathakanon, C., 1988. Early diagenesis of organic matter in Peru continental margin sediments: phosphorite precipitation. Mar. Geol. 80, 309–343.

Gallarday, T., 2009. Fosfatos en la zona Ocucaje, sur de Ica–Perú. Revista del Instituto de Investigación de la Facultad de Ingeniería Geológica, Minera. Metalúrgica y Geográfica 12, 33–42.

Gallardo, V.A., 1977. Large benthic microbial communities in sulphide biota under Peru–Chile subsurface countercurrent. Nature 268, 331–332.

Gao, P., He, Z., Li, S., Lash, G.G., Li, B., Huang, B., Yan, D., 2018. Volcanic and hydrothermal activities recorded in phosphate nodules from the Lower Cambrian Niutitang Formation black shales in South China. Palaeogeogr. Palaeoclimatol. Palaeoecol. 505, 381–397.

Gariboldi, K., Gioncada, A., Bosio, G., Malinverno, E., Di Celma, C., Tinelli, C., Cantalamessa, G., Landini, W., Urbina, M., Bianucci, G., 2015. The dolomite nodules enclosing fossil marine vertebrates in the East Pisco Basin, Peru: field and petrographic insights into the Lagerstätte formation. Palaeogeogr. Palaeoclimatol. Palaeoecol. 438, 81–95.

Gariboldi, K., Bosio, G., Malinverno, E., Gioncada, A., Di Celma, C., Villa, I.M., Urbina, M., Bianucci, G., 2017. Biostratigraphy, geochronology and sedimentation rates of the upper Miocene Pisco Formation at two important marine vertebrate fossil-bearing sites of southern Peru. Newsl. Stratigr. 50, 417–444. https://doi.org/10.1127/nos/2017/0345.

Garrison, R.E., Kastner, M., 1990. Phosphatic sediments and rocks recovered from the Peru margin during ODP Leg 112. Proc. Ocean Drill. Progr. Sci. Results 112, 111–134.

Garrison, R., 1992. Neogene phosphogenesis along the eastern margin of the pacific ocean. Rev. Geol. Chile 19 (1), 91–111.

Garzanti, E., 1993. Himalayan ironstones," superplumes," and the breakup of Gondwana. Geology 21, 105–108.

Glenn, C.R., 1990. Pore Water, Petrologic and Stable Carbon Isotopic Data Bearing on the Origin of Modern Peru Margin Phosphorites and Associated Authigenic Phases. Neogene to Recent Phosphorite. Cambridge University Press, pp. 46–61.

Glenn, C.R., Arthur, M.A., 1988. Petrology and major element geochemistry of Peru margin phosphorites and associated diagenetic minerals: authigenesis in modern organic-rich sediments. Mar. Geol. 80, 231–267.

Glenn, C.R., Föllmi, K.B., Riggs, S.R., Baturin, G.N., Grimm, K.A., Trappe, J., Abed, A.M., Galli-Oliver, C., Garrison, R.E., Ilyin, A.V., Jehl, C., Rohrlich, V., Sadaqah, R.M.Y., Schidlowski, M., Sheldon, R.E., Siegmund, H., 1994. P and phosphorites: sedimentology and environments of formation. Eclogae Geologicae Helveticae 87, 747–788.

Govindaraju, K., 1980. Report (1980) on three GIT-IWG rock reference samples: Anorthosite from Greenland, AN-G; Basalte d'Essey-la-Côte, BE-N; Granite de Beauvoir, MA-N. Geostand. Newsl. 4, 49–138.

Govindaraju, K., 1994. 1994 compilation of working values and sample description for 383 geostandards. Geostand. Newsl. 18, 1–158.

Grohol, M., Veeh, C., 2023. Study on the Critical Raw Materials for the EU 2023. Final Report DG GROW.

Haley, B.A., Klinkhammer, G.P., McManus, J., 2004. Rare earth elements in porewaters of marine sediments. Geochem. Cosmochim. Acta 68 (6), 1265–1279.

Herbozo, G., Kukowski, N., Clift, P.D., Pecher, I., Bolaños, R., 2020. Cenozoic increase in subduction erosion during plate convergence variability along the convergent margin off Trujillo, Peru. Tectonophysics 790, 228557. https://doi.org/10.1016/j.tecto.2020.228557.

Jaisi, D.P., Blake, R.E., 2010. Tracing sources and cycling of phosphorus in Peru Margin sediments using oxygen isotopes in authigenic and detrital phosphates. Geochem. Cosmochim. Acta 74, 3199–3212.

Jørgensen, B.B., Gallardo, V.A., 1999. *Thioploca* spp.: filamentous sulfur bacteria with nitrate vacuoles. FEMS Microbiol. Ecol. 28, 301–313.

Kazakov, A.V., 1937. The phophorite facies and the genesis of phosphorites. Trans. Sci. Fertil. Insecto-fungicides 142, 95–113.

Kidwell, S.M., 1989. Stratigraphic condensation of marine transgressive records: origin of major shell deposits in the Miocene of Maryland. J. Geol. 97, 1–24.

Kulm, L.D., Resig, J.M., Thornburg, T.M., Schrader, H.J., 1982. Cenozoic structure, stratigraphy and tectonics of the central Peru forearc. In: Legget, J.K. (Ed.), Trench and Forearc Geology: Sedimentation and Tectonics on Modern and Ancient Plate Margins Blackwell, pp. 151–169. https://doi.org/10.1144/GSL.SP.1982.01.

Lambert, O., Godfrey, S.J., Fitzgerald, E.M., 2018. *Yaquinacetus meadi*, a new latest oligocene–early miocene dolphin (cetacea, odontoceti, squaloziphiidae, fam. Nov.) from the nye mudstone (Oregon, USA). J. Vertebr. Paleontol. 38, e1559174.

Lisson, C., 1898. Los fosfatos de Ocucaje: Boletín de Minas. Industrias y Construcciones 14, 49–53.

MacDonald, G.H., 1956. Miocene of the Sechura desert, piura. Bol. Soc. Geol. Peru 30.

MacEachern, J.A., Raychaudhuri, I., Pemberton, S.G., 1992. Stratigraphic applications of the *Glossifungites ichnofacies*: delineating discontinuities in the rock record. In: Pemberton, S.G. (Ed.), Applications of Ichnology to Petroleum Exploration. Society of Economic Paleontologists and Mineralogists, pp. 169–198. Core Workshop Notes, 17.

Malinverno, E., Bosio, G., Di Celma, C., Gariboldi, K., Gioncada, A., Pierantoni, P.P., Collareta, A., Molli, G., Bagnoli, G., Sarti, G., Urbina, M., Bianucci, G., 2021. (Bio) stratigraphic overview and paleoclimatic-paleoceanographic implications of the middle-upper Eocene deposits from the Ica River valley (East Pisco basin, Peru). Palaeogeogr. Palaeoclimatol. Palaeoecol. 578, 11056 https://doi.org/10.1016/j.palaeo.2021.110567.

Malinverno, E., Bosio, G., Gioncada, A., Cimò, R., Andò, S., Mariani, L., Coletti, G., Boschi, C., Gariboldi, K., Galimberti, L., Bianucci, G., Urbina, M., Di Celma, C., 2023. Laterally-continuous dolomite layers of the Miocene Pisco Formation (East Pisco Basin, Peru): a window into past cyclical changes of the diagenetic environment. Mar. Petrol. Geol. 147, 105977.

Manheim, F., Rowe, G.T., Jipa, D., 1975. Marine phosphorite formation off Peru. J. Sediment. Res. 45, 243–251.

Marshall-Neill, G., Ruffell, A., 2004. Authigenic phosphate nodules (Late Cretaceous, northern Ireland) as condensed succession microarchives. Cretac. Res. 25, 439–452.

Marty, R.C., 1989. Stratigraphy and Chemical Sedimentology of Cenozoic Biogenic Sediments from the Pisco and Sechura Basins. Rice University, Peru. PhD Thesis.

Marty, R.C., Dunbar, R.B., Allen, M.R., Martin, J.B., Baker, P.A., 1987. Late Miocene biogenic sediments from northern Peru: a Monterey Formation analogue deposited in a shoaling basin. In: Barron, J.A., Blueford, J.R. (Eds.), Abstracts Vol. 4th Int. Congr. Pacific Neogene Stratigr, pp. 70–71.

McArthur, J.M., 1983. Offshore Peruvian phosphorite: a reappraisal of its age and genesis. Chem. Geol. 38, 93–105.

McArthur, J.M., Sahami, A.R., Thirlwall, M., Hamilton, P.J., Osborn, A.O., 1990. Dating phosphogenesis with strontium isotopes. Geochem. Cosmochim. Acta 54, 1343–1351.

Noda, A., 2016. Forearc basins: types, geometries, and relationships to subduction zone dynamics. Geol. Soc. Am. Bull. 128 (1), 879–895. https://doi.org/10.1130/B31345.

Notholt, A.J.G., Sheldon, R.P., Davidson, D.F., 1989. Phosphate Deposits of the World, Volume 2, Phosphate Rock Resources. Cambridge University Press, Cambridge, p. 566.

Papineau, D., 2010. Global biogeochemical changes at both ends of the Proterozoic: insights from phosphorites. Astrobiology 10, 165–181.

Pemberton, S.G., MacEachern, J.A., Saunders, T., 2004. Stratigraphic Applications of Substrate-specific Ichnofacies: Delineating Discontinuities in the Rock Record, vol. 228. Geological Society, London, Special Publications, pp. 29–62.

Petrash, D.A., Bialik, O.M., Bontognali, T.R., Vasconcelos, C., Roberts, J.A., McKenzie, J. A., Konhauser, K.O., 2017. Microbially catalyzed dolomite formation: from near-surface to burial. Earth Sci. Rev. 171, 558–582.

Piper, D.Z., Baedecker, P.A., Crock, J.G., Burnett, W.C., Loebner, B.J., 1988. Rare earth elements in the phosphatic-enriched sediment of the Peru shelf. Mar. Geol. 80, 269–285.

Pufahl, P.K., Grimm, K.A., 2003. Coated phosphate grains: proxy for physical, chemical, and ecological changes in seawater. Geology 31, 801–804.

Pufahl, P.K., Groat, L.A., 2016. Sedimentary and igneous phosphate deposits: formation and exploration: an invited paper. Bulletin of the Society of Economic Geologists 112, 483–516.

Pufahl, P.K., Grimm, K.A., Abed, A.M., Sadaqah, R.M., 2003. Upper Cretaceous (Campanian) phosphorites in Jordan: implications for the formation of a south Tethyan phosphorite giant. Sediment. Geol. 161, 175–205.

Reynard, B., Balter, V., 2014. Trace elements and their isotopes in bones and teeth: diet, environments, diagenesis, and dating of archeological and paleontological samples.

Palaeogeogr. Palaeoclimatol. Palaeoecol. 416, 4–16. https://doi.org/10.1016/j.palaeo.2014.07.038.
Reynaud, J.Y., James, N.P., 2012. The Miocene Sommières basin, SE France: bioclastic carbonates in a tide-dominated depositional system. Sediment. Geol. 282, 360–373.
Rismyhr, B., Bjærke, T., Olaussen, S., Mulrooney, M.J., Senger, K., 2018. Facies, palynostratigraphy and sequence stratigraphy of the wilhelmøya subgroup (upper triassic–middle jurassic) in western central spitsbergen, svalbard. Nor. Geol. Tidsskr. 99, 35–64.
Romero, D., Valencia, K., Alarcón, P., Peña, D., Ramos, V.A., 2013. The offshore basement of Peru: evidence for different igneous and metamorphic domains in the forearc. J. S. Am. Earth Sci. 42, 47–60. https://doi.org/10.1016/j.jsames.2012.11.003.
Ruttenberg, K.C., Berner, R.A., 1993. Authigenic apatite formation and burial in sediments from non-upwelling, continental margin environments. Geochem. Cosmochim. Acta 57, 991–1007.
Salama, W., El-Kammar, A., Saunders, M., Morsy, R., Kong, C., 2015. Microbial pathways and palaeoenvironmental conditions involved in the formation of phosphorite grains, Safaga District, Egypt. Sediment. Geol. 325, 41–58.
Saltzman, M.R., 2003. Organic carbon burial and phosphogenesis in the Antler foreland basin: an out-of-phase relationship during the Lower Mississippian. J. Sediment. Res. 73, 844–855.
Schulz, H.N., Schulz, H.D., 2005. Large sulfur bacteria and the formation of phosphorite. Science 307 (5708), 416–418.
Sheldon, R.P., 1981. Ancient marine phosphorites. Annu. Rev. Earth Planet Sci. 9, 251–284. https://doi.org/10.1146/annurev.ea.09.050181.001343.
Slomp, C.P., Thomson, J., de Lange, G.J., 2002. Enhanced regeneration of phosphorus during formation of the most recent eastern Mediterranean sapropel (S1). Geochem. Cosmochim. Acta 66, 1171–1184.
Smrzka, D., Zwicker, J., Schulz-Vogt, H., Little, C.T., Rieder, M., Meister, P., Gier, S., Peckmann, J., 2024. Fossilized giant sulfide-oxidizing bacteria from the Devonian Hollard Mound seep deposit, Morocco. Geobiology 22, e12581.
Soudry, D., Lewy, Z., 1988. Microbially influenced formation of phosphate nodules and megafossil moulds (Negev, southern Israel). Palaeogeogr. Palaeoclimatol. Palaeoecol. 64, 15–34.
Suess, E., 1981. Phosphate regeneration from sediments of the Peru continental margin by dissolution of fish debris. Geochem. Cosmochim. Acta 45, 577–588.
Suits, N.S., Arthur, M.A., 2000. Bacterial production of anomalously high dissolved sulfate concentrations in Peru slope sediments: steady-state sulfur oxidation, or transient response to end of El Niño? Deep-Sea Res Pt I 47, 1829–1853.
Thornburg, T.M., Kulm, L.D., 1981. Sedimentary basins of the Peru continental margin: structure, stratigraphy, and Cenozoic tectonics from 6°S to 16°S latitude. In: Kulm, L. D., Dymond, J., Dasch, E.J., Hussong, D.M. (Eds.), Nazca Plate: Crustal Formation and Andean Convergence, vol. 154. Geological Society of America, Memoir, pp. 393–422.
Veeh, H.H., Burnett, W.C., Soutar, A., 1973. Contemporary phosphorites on the continental margin of Peru. Science 181, 844–845.
Viveen, W., Schlunegger, F., 2018. Prolonged extension and subsidence of the Peruvian forearc during the Cenozoic. Tectonophysics 730, 48–62. https://doi.org/10.1016/j.tecto.2018.02.018.
Von Huene, R., Suess, E., 1988. Ocean drilling program Leg 112, Peru continental margin. Geology 16, 934–938.
Whitney, D.L., Evans, B.W., 2010. Abbreviations for names of rock-forming minerals. Am. Mineral. 95, 185–187.
Zecchin, M., Catuneanu, O., Caffau, M., 2019. Wave-ravinement surfaces: classification and key characteristics. Earth Sci. Rev. 188, 210–239.
Zegarra, J., Canales, H., 2013. Exploración de fosfatos en el Perú y su implicancia a nivel mundial. Bol. Soc. Geol. Peru 107, 176–179.
Zen, E.A., 1959. Mineralogy and petrography of marine bottom sediment samples off the coast of Peru and Chile. J. Sediment. Res. 29, 513–539.
Zopfi, J., Böttcher, M.E., Jørgensen, B.B., 2008. Biogeochemistry of sulfur and iron in Thioploca-colonized surface sediments in the upwelling area off central Chile. Geochem. Cosmochim. Acta 72 (3), 827–843.